

# In Situ Covalent Reinforcement of a Benzene-1,3,5-Tricarboxamide Supramolecular Polymer Enables Biomimetic, Tough, and Fibrous Hydrogels and Bioinks


Shahzad Hafeez, Monize Caiado Decarli, Agustina Aldana, Mahsa Ebrahimi, Floor A.A. Ruitter, Hans Duimel, Clemens van Blitterswijk, Louis M. Pitet, Lorenzo Moroni, and Matthew B. Baker\*

Synthetic hydrogels often lack the load-bearing capacity and mechanical properties of native biopolymers found in tissue, such as cartilage. In natural tissues, toughness is often imparted via the combination of fibrous noncovalent self-assembly with key covalent bond formation. This controlled combination of supramolecular and covalent interactions remains difficult to engineer, yet can provide a clear strategy for advanced biomaterials. Here, a synthetic supramolecular/covalent strategy is investigated for creating a tough hydrogel that embodies the hierarchical fibrous architecture of the extracellular matrix (ECM). A benzene-1,3,5-tricarboxamide (BTA) hydrogelator is developed with synthetically addressable norbornene handles that self-assembles to form a and viscoelastic hydrogel. Inspired by collagen's covalent cross-linking of fibrils, the mechanical properties are reinforced by covalent intra- and interfiber cross-links. At over 90% water, the hydrogels withstand up to 550% tensile strain, 90% compressive strain, and dissipated energy with recoverable hysteresis. The hydrogels are shear-thinning, can be 3D bioprinted with good shape fidelity, and can be toughened via covalent cross-linking. These materials enable the bioprinting of human mesenchymal stromal cell (hMSC) spheroids and subsequent differentiation into chondrogenic tissue. Collectively, these findings highlight the power of covalent reinforcement of supramolecular fibers, offering a strategy for the bottom-up design of dynamic, yet tough, hydrogels and bioinks.

## 1. Introduction

Regenerative medicine and tissue engineering have the potential to change the way we treat disease and degeneration. Advancements in cellular reprogramming, organoids, synthetic biology, and 3D fabrication technologies have revolutionized the field in the past 10 years; yet, our struggle to recreate life-like mimics of the extracellular matrix (ECM) slows progress. The ECM around a cell provides a dynamic environment for spatiotemporal and reciprocal interactions (e.g., signaling, mechanical properties) with other cells and tissue.<sup>[1]</sup> This recapitulation of ECM complexity is imperative to create environments that can effectively communicate with living cells,<sup>[2]</sup> impacting applications including tissue engineering, implants, biosensors, and sustainable materials. Incorrect communication can lead to, for example, cells committing to the wrong lineage, death of the cells, improper immune response, or insufficient maturation, which can shut down tissue regeneration or block the desired function of the device or organism.

S. Hafeez, M. C. Decarli, A. Aldana, F. A. Ruitter, C. van Blitterswijk, L. Moroni, M. B. Baker  
Department of Complex Tissue Regeneration  
MERLN Institute for Technology-Inspired Regenerative Medicine  
Maastricht University  
P.O. Box 616, Maastricht 6200 MD, The Netherlands  
E-mail: m.baker@maastrichtuniversity.nl

 The ORCID identification number(s) for the author(s) of this article can be found under <https://doi.org/10.1002/adma.202301242>

© 2023 The Authors. Advanced Materials published by Wiley-VCH GmbH. This is an open access article under the terms of the Creative Commons Attribution License, which permits use, distribution and reproduction in any medium, provided the original work is properly cited.

DOI: 10.1002/adma.202301242

M. Ebrahimi, L. M. Pitet  
Advanced Functional Polymers Group  
Department of Chemistry  
Institute for Materials Research (IMO)  
Hasselt University  
Martelarenlaan 42, Hasselt 3500, Belgium

F. A. Ruitter  
Department of Cell Biology-Inspired Tissue Engineering  
MERLN Institute for Technology-Inspired Regenerative Medicine  
Maastricht University  
P.O. Box 616, Maastricht 6200 MD, The Netherlands  
H. Duimel  
Maastricht MultiModal Molecular Imaging Institute  
P.O. Box 616, Maastricht 6200 MD, The Netherlands

Hydrogels are important for many biological applications, due to their ability to mimic many of the properties of the native ECM.<sup>[3]</sup> Key to this function is not only the biomimetic nature (stiffness, bioactivity) of a designed hydrogel, but also the importance of dynamic properties of hydrogels has recently emerged. For example, studies on synthetic materials clearly show that enzymatic degradation,<sup>[4]</sup> stress-stiffening,<sup>[5]</sup> and stress-relaxation<sup>[6,7]</sup> have major effects on tissue formation. We now know that dynamic mechanical properties are imperative for controlling stem cell differentiation,<sup>[6]</sup> improving organoid culture,<sup>[8]</sup> enhancing neural regeneration,<sup>[9]</sup> and controlling cell fate.<sup>[10]</sup> Despite these breakthroughs, poor mechanical properties, and lack of hierarchical complexity in these hydrogels must be addressed.<sup>[11]</sup>

Current synthetic hydrogels rely largely on either covalent (static and strong) or dynamic (transient and weak) cross-linking. By contrast, natural assemblies rely on both covalent and dynamic (supramolecular) interactions. Tissues such as cartilage, muscles, tendons, and ligaments exhibit remarkable toughness, elasticity, and fast recovery.<sup>[12]</sup> The exceptional mechanical properties of many tissues are often attributed to the hierarchical fibril macromolecular structure. An excellent example of this hierarchical structure, collagen is the backbone of many tough tissues. Collagen fibrils are composed of a self-assembled structure of tropocollagen, mainly driven by noncovalent interactions. These supramolecular fibrils are further stabilized by intra- and intermolecular covalent cross-links (via aldol condensation and aldimine cross-links).<sup>[13]</sup> Theoretical and molecular modeling studies suggest that intermolecular hydrogen-bonding interactions and permanent cross-links between the collagen fibrils are mainly responsible for the impressive mechanical properties and toughness.<sup>[14]</sup> In numerous biological assemblies, we can observe the powerful coevolution of covalent and supramolecular interactions. For example, the self-assembly of tropoelastin into fibrous elastin, driven by lysine forming bifunctional and tetrafunctional cross-links,<sup>[15,16]</sup> and  $\alpha$ -actinin forming cross-links between actin filaments.<sup>[17]</sup> To overcome the limitations of poor mechanical properties in soft hydrogels, several synthetic strategies for forming tough hydrogels are emerging and include double networks<sup>[18–20]</sup> dual cross-linking (covalent bonds and H-bonding),<sup>[21]</sup> conjoined networks,<sup>[22]</sup> sacrificial H-bonding interactions,<sup>[23,24]</sup> force-triggered reactive strand extension,<sup>[25]</sup> and dense entanglements.<sup>[26,27]</sup> However, the biomimetic strategy of combining supramolecular structure with key covalent bond formation has not been thoroughly studied in synthetic systems.

Supramolecular chemistry has rapidly advanced, enabling the rational design of hierarchical and functional materials (vaccines, drug delivery, biomaterials<sup>[28–31]</sup>). Collagen has served as an inspiration to the supramolecular chemist, and classic studies show our ability to partially recreate its structure from synthetic components.<sup>[32]</sup> Though recently postulated,<sup>[33]</sup> there are surprisingly few studies on the modification of supramolecular assemblies via postassembly covalent modifications. Recent studies combining supramolecular nanofibers with covalent networks have created impressive materials and artificial muscles.<sup>[34–36]</sup> Others have briefly studied the synergy of supramolecular and covalent bonds in hydrogels<sup>[37–40]</sup> and some via dual-network approaches.<sup>[41]</sup> In other examples, fibrous protein-based hydrogels, which undergo force-induced unfolding, has been shown

as a novel toughening mechanism.<sup>[42]</sup> Several groups have recently reported cross-linking of fibrous assemblies either to create a reversible robust hydrogel<sup>[43]</sup> or enhance mechanical properties.<sup>[39,44–48]</sup> A tough hydrogel through tandem supramolecular and covalent cross-linking has also been reported; however, the hydrogel is made up of a double network lacking 1D self-assembly.<sup>[49]</sup> Despite these initial attempts, introducing functionality and toughness under cytocompatible conditions in a processable material is rare. This lack of knowledge is juxtaposed with nature's consistent use of the strategy to build functional materials.

Self-assembling supramolecular and dynamic hydrogels are attractive candidates for 3D printing with living cells,<sup>[50]</sup> due to the benefits of the creation of multiscale hierarchically controlled systems, being mechanically tunable, self-healing, and shear-thinning.<sup>[51]</sup> The 3D bioprinting of hydrogels has been used to fabricate complex tissue-like structures such as heart valves,<sup>[52,53]</sup> vascular networks,<sup>[54–57]</sup> corneal domes,<sup>[58]</sup> and kidneys.<sup>[59]</sup> Yet, balancing the dynamics of a hydrogel with stability and toughness has created additional challenges toward bioprinting complex 3D life-like structures. Consequently, most of the bioinks developed are only marginally suited for extrusion bioprinting since they are highly viscous liquids,<sup>[60]</sup> can sediment cells at the bottom of ink cartridges, block the nozzle owing to fast ultra-violet (UV) cross-linking,<sup>[41]</sup> involve large pH shifts (for collagen gels), or have supraphysiological levels of calcium ions (e.g., for alginate bioinks). Shear-thinning hydrogels have clearly been shown to increase cell viability during bioprinting,<sup>[61]</sup> and this property has been rationally designed using dynamic covalent bonds<sup>[62,63]</sup> and supramolecular host-guest interactions.<sup>[64–66]</sup> Recent reports showed the engineering of shear-thinning and 3D printing of self-assembled fibrous peptide amphiphiles,<sup>[67]</sup> peptide inks,<sup>[68,69]</sup> and BTAs;<sup>[70]</sup> however, designing a synthetic biomimetic bioink with 1D self-assembled fibers that possess both shear-thinning and remarkable toughness remains a formidable challenge.

To create a biomimetic, tough, and processable hydrogel, we took inspiration from nature's conjunction of self-assembly and covalent reinforcement. We designed a benzene-1,3,5-tricarboxamide (BTA) hydrogelator with norbornene (NB) functional handles that we surmised could self-assemble into 1D fibrils. We hypothesized that these biomimetic supramolecular assemblies could be fixed/cross-linked, ultimately leading to a tough hydrogel via intra- and interfiber cross-links. Via rheology and mechanical testing (compression and tensile), we discovered that the toughness, stiffness, and strength of the hydrogels could be tuned in biologically relevant regimes. Ultimately, this supramolecular-co-covalent strategy allowed the creation of remarkably tough 3D bioinks, which were explored for the 3D printing of an in vitro cartilage tissue model.

## 2. Results and Discussion

### 2.1. Molecular Design and NB BTA Synthesis

We designed the norbornene BTA (NB BTA) macromonomer with norbornene functionalities on the two outer ends of a telechelic BTA polyethylene glycol (**Figure 1a**). The hydrophobic nature of the norbornene, in combination with a dodecane

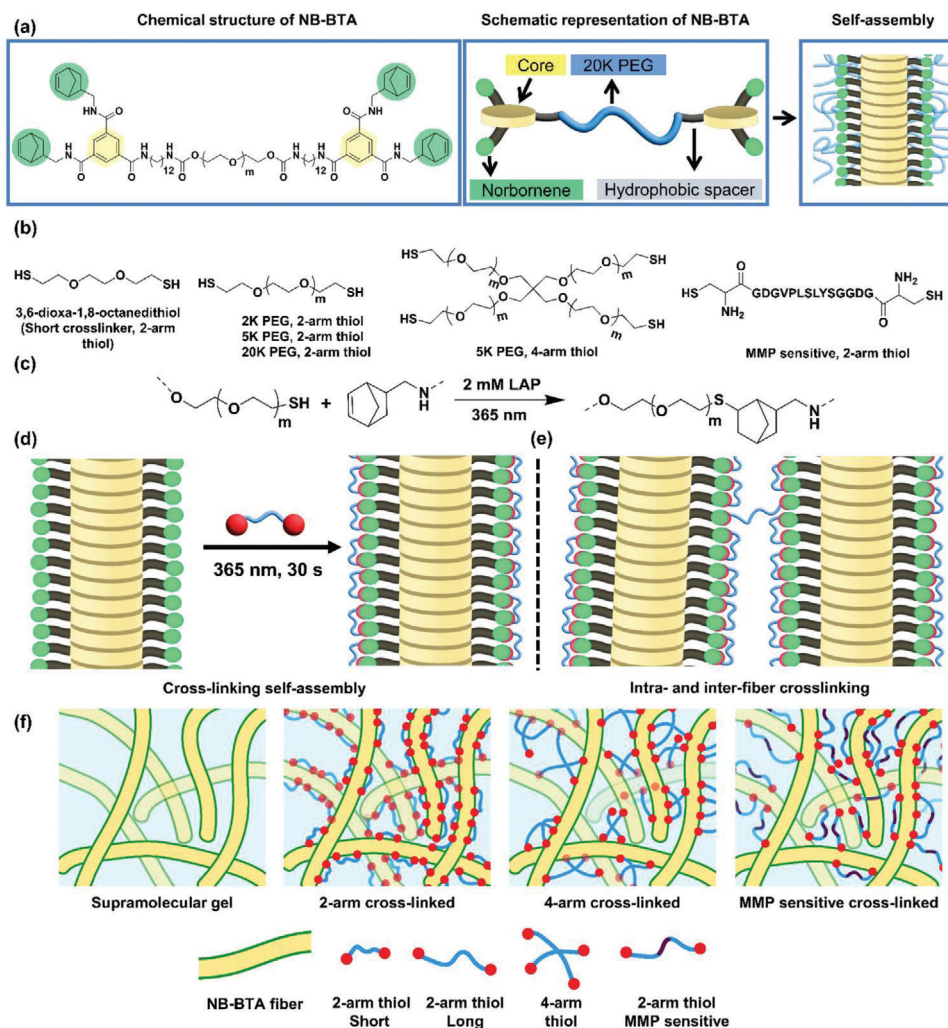


**Figure 1.** Molecular structures of NB BTA and cross-linkers employed in the study. a) Chemical structure of norbornene functionalized NB BTA macromonomer. Cartoon representation of NB BTA macromonomer and proposed stacking of NB BTA macromonomer (middle) to form a fiber (right). Blue chains represent 20K PEG. b) Thiol cross-linkers utilized for cross-linking supramolecular assemblies. c) Reaction scheme for thiol-ene chemistry of norbornene and thiol. d) Cartoon of supramolecularly self-assembled fiber cross-linked using short dithiol cross-linker. e) Intra- and interfiber cross-linking at molecular level. 20K PEG chains were not shown in (d) and (e) to clearly demonstrate cross-linking of the supramolecular fiber. f) Schematic of the supramolecular hydrogel network (left), after cross-linking with a short 2-arm thiol cross-linker (middle left), 4-arm thiol cross-linker (middle right), and MMP sensitive 2-arm thiol cross-linker (right). The green border on a supramolecular fiber represents the norbornene.

internal spacer,<sup>[71]</sup> was envisioned to provide a hydrophobic pocket upon self-assembly, while the poly(ethylene glycol) (PEG) would provide good water miscibility. The unsaturated norbornene would also serve as a functional handle on the macromonomer, enabling functionalization using the thiol-ene reaction. With a previously reported desymmetrization strategy,<sup>[72]</sup> the dinorbornene BTA synthon was readily obtained by desymmetrizing a benzene-1,3,5-triester (tris(perfluorophenyl) benzene-1,3,5-tricarboxylate, BTE-F<sub>5</sub>Ph) with two equivalents of 5-norbornene 2-methylamine (Figure S1, Supporting Information). The target NB BTA macromonomer was synthesized by covalently connecting two dinorbornene BTA synthon molecules to amine-terminated PEG (20 kg mol<sup>-1</sup>, PEG20K) (Figure S1, Supporting Information). We successfully synthesized the pure macromonomer (<sup>1</sup>H NMR Figure S2, Sup-

porting Information) with an average molecular weight of  $\approx 23$  kg mol<sup>-1</sup> and dispersity of 1.2 ( $\mathcal{D}$ , gel permeation chromatography, Figure S3, Supporting Information). Schematics of the NB BTA macromonomer, self-assembly, thiol-ene chemistry, and inter- and intrafiber cross-linking using different thiol cross-linkers are shown in Figure 1b–f.

## 2.2. NB BTA Aggregates to form a Fibrillar Morphology

The self-assembly of the NB BTA macromonomer was first investigated in an aqueous environment by dissolution in a minimal amount of methanol and assembly via injection into water. Utilizing the solvatochromic dye Nile Red<sup>[73]</sup> as a reporter, we observed an increase in fluorescence, consistent with the

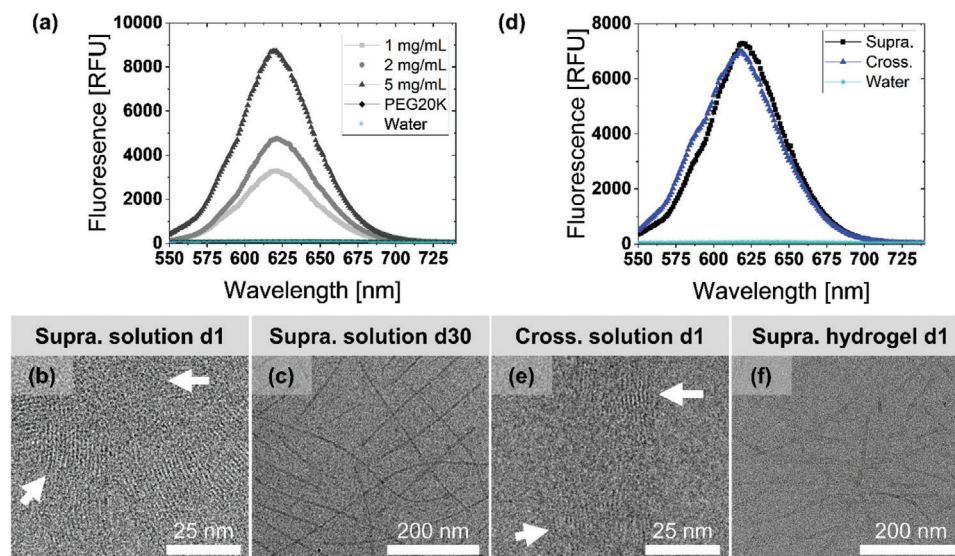


**Figure 2.** Self-assembly studies. a) Nile red fluorescence as a function of NB BTA concentration in water. b) Nanofibres of NB BTA at  $10 \text{ mg mL}^{-1}$  as observed via cryo-TEM. c) Supramolecular fibers in dilute solutions at  $5 \text{ mg mL}^{-1}$  aged for 30 d showed nanofiber bundles with a diameter around 5 nm. d) Nile red fluorescence for cross-linked versus non-crosslinked (supramolecular) NB BTA solutions at  $5 \text{ mg mL}^{-1}$ . e) the supramolecular structure is still observed by cryo-TEM after exposure to UV light ( $365 \text{ nm}$  at  $\approx 1 \text{ mW cm}^{-2}$ ) for cross-linking. f) A dissolved supramolecular hydrogel (to  $5 \text{ mg mL}^{-1}$ ) also showed bundles of fibrils around 10–15 nm in diameter.

formation of a hydrophobic pocket.<sup>[74]</sup> The fluorescence intensity increased with increasing hydrogelator concentration from 1, 2, and 5 milligram per millilitre ( $\text{mg mL}^{-1}$ ), which suggested an increasing volume of the hydrophobic pocket (Figure 2a). The fluorescence intensity wavelength ( $\lambda_{\text{max}}$ ,  $\approx 620 \text{ nm}$ ) remained constant for all tested concentrations and was blue-shifted compared to a PEG20K solution in water (Figure S4, Supporting Information). The blue shift suggests a nonpolar environment and the similar  $\lambda_{\text{max}}$  pointed to a consistent strength of the hydrophobic pocket at all concentrations. These observations are in line with previously reported 1D fibrous BTA structures with aliphatic hydrophobic spacers and gave us confidence that we had a well-behaved supramolecular assembly within a range of accessible concentrations.<sup>[72]</sup>

In order to gain structural information on this self-assembly, we investigated the self-assembled NB BTA macromonomer (at  $10 \text{ mg mL}^{-1}$ ) with cryo-transmission electron microscopy (cryo-TEM). Cryo-TEM revealed NB BTA superstructures, the size of which presumably points to the formation of bundled, parallel nanofibers in samples that had been aged between 16–24 h (Figure 2b; Figure S5, Supporting Information). A single nanofiber measured  $\approx 1.5 \text{ nm}$  in diameter, and the bundles varied between 15 and 60 nm in diameter. Nanofiber bundling is likely due to hydrophobic interactions between BTA molecules. Next, an aged sample was examined after 30 d ( $5 \text{ mg mL}^{-1}$ , Figure 2c). Immediately apparent are the high-aspect-ratio fibers formed in these samples. The ageing of NB BTA resulted in the evolution of fingerprint-like bundles into well-defined fibers, characterized by diameters ranging from 5 nm to 15–50 nm. The length of the nanofibers varied between a couple of hundred nanometers to a micrometer. Aging the samples further did not provide significant differences, as similar dimensions were observed after 270 d (Figure S6, Supporting Information).

### 2.3. The Self-Assembled NB BTA Retained the Hydrophobic Pocket and Fibrillar Morphology after Cross-Linking

Having established hydrophobic pocket formation and fibrous morphology, we next tested if the self-assembled NB BTA structures underwent major changes to the hydrophobic pocket after being subjected to cross-linking conditions ( $2 \times 10^{-3} \text{ M}$  lithium phenyl-2,4,6-trimethylbenzoylphosphinate, LAP, photoinitiator, 365 nm UV light and  $\approx 1 \text{ mW cm}^{-2}$  for 1–4 min). Using a short (8-atoms) dithiol cross-linker, we cross-linked a dilute solution of the macromonomer. This cross-linked NB BTA displayed similar Nile Red fluorescence to the non-crosslinked controls both in intensity and  $\lambda_{\text{max}}$  (Figure 2d). Neither red nor blue shift was detected, which suggests that the polarity of the hydrophobic pocket was not majorly affected by the cross-linking reaction. The fixed supramolecular assemblies were further probed by cryo-TEM to examine any potential structural changes after the covalent cross-linking. No changes were observed in the structure or fibrillar morphology on the micron and 10 s of nm scale. (Figure 2e; Figure S5, Supporting Information). With this knowledge in hand, we subsequently pursued uncovering the potential of these macromonomers as hydrogel materials.

### 2.4. Formation and Cross-Linking of Hydrogels from Supramolecular NB BTA

Next, we were interested to investigate the ability of the synthesized NB BTA macromonomer to form hydrogels in water at different concentrations (2.5, 5.0, 7.5, and 10% w/v). Hydrogel formation was confirmed at all tested concentrations via the vial inversion test (Figure S7, Supporting Information). The lower-concentration hydrogels were qualitatively soft and fragile with

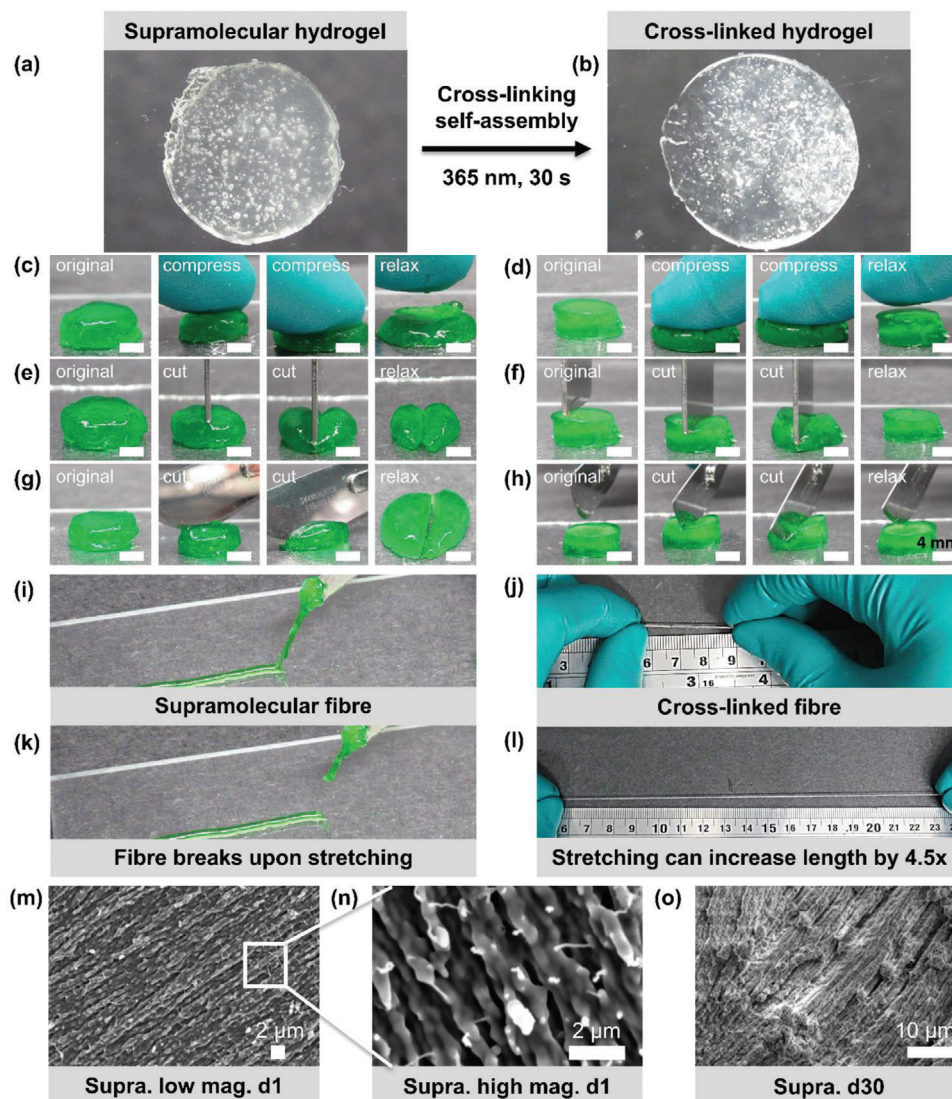


**Figure 3.** Cross-linking of the supramolecular hydrogel leads to strong, tough, and stretchable hydrogels. a–g) Optical image of NB BTA hydrogel at 5% w/v before (a) and after (b) cross-linking. c–h) Optical images of supramolecular and cross-linked hydrogel under extreme compression (c vs d), cutting of the hydrogel using a spatula (e vs f), and cutting using a scalpel (g vs h). i) Stretching of extruded supramolecular (i and k) and cross-linked filament (j and l). The supramolecular filament broke while the cross-linked filament can be stretched to 4.5× (450% strain) of its original length. m–o) The supramolecular hydrogel (50 mg mL<sup>-1</sup>) showed anisotropic fibrillar morphology via cryo-SEM at low (m) and high (n) magnification, and the hydrogel aged for 30 d (o) showed aligned bundle of fibers.

increasing stiffness upon increasing concentration. In order to quickly test the feasibility of the cross-linking approach in the hydrogel, the hydrogels were cross-linked with a short dithiol after equilibration at room temperature for  $\approx 2$  h (LAP, 365 nm for 30–60 s, **Figure 3a,b**, **Figure S7**, Supporting Information). Immediately, we noticed that all concentrations transitioned from fragile samples to remarkably tough, stretchable materials and offered resistance to cutting with a spatula (Movies S1–S4, Supporting Information).

We then further investigated the macroscopic properties of the 5% w/v hydrogel before and after cross-linking with the short dithiol at a 1:1 ratio of [NB]:[thiol] (**Figure 3**). While both the non-crosslinked and cross-linked hydrogels were compressible using a finger, the cross-linked hydrogel showed immediate

recovery upon removing the force (**Figure 3c,d**). Then we compressed the cross-linked hydrogel using a spatula and the hydrogel resisted a considerable load before cracking (**Figure S8**, Supporting Information). Next, we compared the cutting of the supramolecular versus cross-linked hydrogels using first a spatula and then a sharp scalpel; the supramolecular hydrogel could be cut easily using a spatula and scalpel (**Figure 3e,g**) while the cross-linked hydrogel required substantially more effort and was only severed after several cycles of aggressive cutting (**Figure 3f,h**; **Movie S5** in the Supporting Information of scalpel cutting). Furthermore, the supramolecular hydrogels (pre-crosslinking) were able to be extruded into uniform filament shapes (**Figure 3i,k**), indicative of good injectability and potential for 3D printing. After cross-linking, the originally weak filament

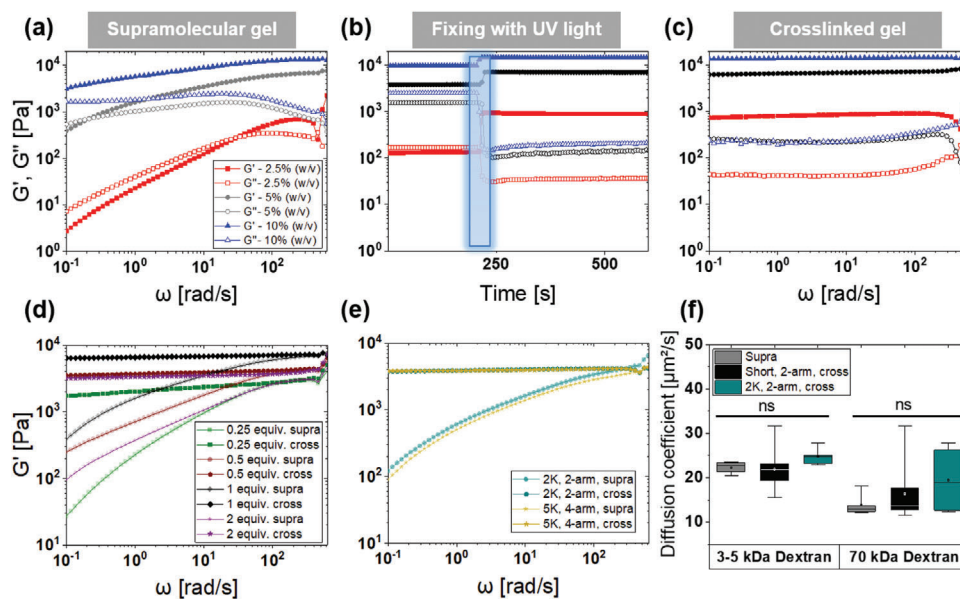


**Figure 4.** Mechanical properties of hydrogels before and after cross-linking. a) Supramolecular hydrogel storage moduli ( $G'$ , filled symbols) and loss moduli ( $G''$ , open symbols) as a function of angular frequency at 2.5%, 5%, and 10% w/v NB BTA. b) Evolution of ( $G'$ , filled symbols) and loss moduli ( $G''$ , open symbols) over time for cross-linking of the supramolecular hydrogel when exposed to a UV-light source. c) Storage moduli ( $G'$ , filled symbols) and loss moduli ( $G''$ , open symbols) as a function of the angular frequency of the cross-linked hydrogels. d,e) Storage moduli as a function of the angular frequency of uncross-linked and cross-linked hydrogels using different mole equivalents of short dithiol cross-linker (d) and using 2arm versus 4arm cross-linkers (e). f) Diffusion coefficients of supramolecular and cross-linked hydrogels using short dithiol and PEG2K cross-linker remain similar before and after cross-linking.

could then be extended to 4.5 times (450% strain) its original length before breaking (Figure 3j,l; Movie S6, Supporting Information). These qualitative changes suggested successful cross-linking and prompted further studies.

## 2.5. The NB BTA Hydrogel Exhibited Fibrous Morphology

Next, the internal structure of the supramolecular hydrogel before cross-linking was probed using cryo-TEM and cryo-SEM in order to gain an understanding of the effects of cross-linking on the fibrous morphology. One supramolecular hydrogel was diluted (a 5% w/v hydrogel diluted to 5 mg mL<sup>-1</sup>) for cryo-TEM, which revealed fibers with a diameter of around 15 nm and lengths of several hundreds of nanometers (Figure 2f; Figure S9, Supporting Information). These diluted supramolecular hydrogel structures closely resembled the aged supramolecular solutions seen in the dilute solution studies (vide supra). The bulk hydrogel microstructure was visualized using cryo-SEM. The supramolecular hydrogel (5% w/v in water) showed bundles of fibers that appeared to be parallel (i.e., anisotropically aligned) (Figure 3m,n; Figure S10, Supporting Information). The supramolecular hydrogel retained this anisotropic alignment and bundled fibril morphology in a sample aged for 30 d at room temperature (Figure 3o; Figure S11, Supporting Information). Despite repeated attempts, we were not able to observe fibrils in the bulk cross-linked hydrogel via cryo-SEM. We observed, unlike in the other samples, a patterned surface; this could suggest that the fracture likely occurred at an ice crystal plane and/or that fibrils are beneath the ice sheet.

## 2.6. Tuning of the Mechanical Properties via Concentration and Cross-Linker Type

With ample evidence for the impressive change in mechanical properties and the conservation of supramolecular structure before/after cross-linking, we turned to the mechanical fine-tuning of these hydrogels. We hypothesized that mechanical tuning could be simply achieved via polymer concentration (2.5–10% w/v). Investigated with shear rheology (Figure 4a), the hydrogels possessed a rather large linear viscoelastic regime up to about 30% strain (Figure S12, Supporting Information). The storage moduli increased monotonically with increasing polymer concentration, indicating an increase in elastic properties of hydrogel which likely is due to increased physical interactions between the fibers. The crossover points during a frequency sweep, which reflects the dynamicity of the supramolecular interactions and the viscous properties of the hydrogel, decreased from 34 rad s<sup>-1</sup> for 2.5% to 0.25 and 0.01 rad s<sup>-1</sup> for 5% and 10% NB BTA hydrogels, respectively (Figure 4a; Figure S12, Supporting Information). Moving of the crossover point to lower frequency can be attributed the decrease in viscous/flow properties of the hydrogel.

After knowing the effect of concentration on the mechanical properties, we wished to explore the in situ thiol-ene cross-linking on a rheometer. Using a short thiol cross-linker in a 1:1 [NB]:[thiol] ratio, all formulations (2.5–10%) cross-linked quickly as indicated via a sharp rise in the storage modulus (below 10 s, 365 nm and  $\approx 10$  mW cm<sup>-2</sup> at 1% strain and 10 rad s<sup>-1</sup>, Figure 4b). Under these conditions, the 2.5% w/v hydrogel was initially a viscous liquid, but gelled rapidly after cross-linking; its storage

modulus increased tenfold to 1 kPa. A twofold increase in storage modulus was observed for 5% w/v and 10% w/v formulations, with final values of 7 and 15 kPa, respectively. Looking into the cross-linked hydrogels further, they showed a plateau storage modulus across almost 4 orders of angular frequency, indicative of their elastic nature. Of considerable note, the plateau moduli for the cross-linked hydrogels are nearly identical to the high-frequency equilibrium storage modulus for the non-crosslinked hydrogels (Figure 4a,c; Figure S12, Supporting Information). This equilibrium storage modulus is generally considered to be the modulus outside of the timescale of materials dynamics and is the modulus representative of the structure of the network. Observing identical moduli before and after cross-linking suggests that the network/structure stayed largely the same; it appeared that the cross-linking mainly shuts down the dynamics and does not alter the network topology heavily. Additionally, we also observed that the cross-linking does not change the self-assembled nanostructure when comparing cryo-TEM images (in dilute solution; vide supra, Figure 2; Figure S5, Supporting Information).

Subsequently, the molar ratio of the thiol cross-linker (0.25, 0.5, 1, and 2 equivalents) was explored as a handle to tune the mechanics of the hydrogel at a constant polymer concentration (5% w/v). All formulations were initially viscoelastic (Figure S13, Supporting Information). However, the equilibrium storage moduli varied with the molar ratio of the thiol cross-linker: from  $\approx 4$  kPa for the lowest and highest (0.25 and 2.0, respectively) molar equivalents, to  $\approx 8$  kPa for 1 molar equivalent. Upon cross-linking the hydrogels followed the common trend in traditional covalent hydrogels of an increase in storage modulus with increasing degree of cross-linking, until equimolar ratios, followed by a drop once the cross-linker is in excess; however, this trend was also observed in the pre-crosslinked samples. All of the hydrogels transitioned to being dominantly elastic after cross-linking (Figure 4d; Figure S13, Supporting Information), and the equilibrium storage modulus of each formulation remained constant, again suggesting that the cross-linking did not significantly change the underlying hydrogel's network.

To probe the effect of cross-linking on the storage modulus, topologically more complex cross-linkers were employed. We compared 5K-PEG-4-arm and 2K-PEG-2-arm variants, keeping the arm length roughly constant. We observed that the 4-arm PEG cross-linked slowly when compared to the 2-arm PEG during rheology. However, both exhibited a similar storage moduli of 4.5 kPa. The similar storage moduli between the two samples indicated that the extra topological cross-link in the 5K-PEG-4arm did not contribute significantly to the modulus of the hydrogel (Figure 4e; Figure S14, Supporting Information) at low strains. This again suggests that the covalent network topology does not appreciably influence the storage modulus at low strains, prompting us to further investigate the effect of cross-linker length on mechanical properties.

We then proceeded to explore the molecular length of the cross-linker and its influence on mechanical properties. In principle, a shorter cross-linker would preferentially form intrafiber connections, while longer cross-linkers could form more inter-fiber cross-links. The hydrogels were cross-linked using dithiols of varying lengths: short, 2K-PEG-2-arm, 5K-PEG-2-arm, and 20K-PEG-2-arm. The molar ratio (1:1 of [NB]:[thiol]) and concentration (5% w/v) were kept constant in all cases. Each sam-

ple showed elastic behavior after cross-linking, and marginal changes in the mechanical properties were observed as a function of length. A delayed speed of cross-linking was observed with an increasing molar mass of the cross-linker, and the moduli of the hydrogels dropped stepwise from  $\approx 8$  kPa for the short thiol cross-linker to 4 kPa for the 20K-PEG-2-arm cross-linker (Figure S15, Supporting Information). The experiments do not support an increase in interfiber cross-linking with the higher lengths, yet do show that the mechanical properties are slightly perturbed by larger polymers. Again, the supramolecular hydrogels (before cross-linking) displayed similar equilibrium storage moduli to the cross-linked hydrogels (Figure S15a–c, Supporting Information). These results further reinforced the observation that the shear moduli of the hydrogel formulations are not dependent on the covalent cross-linker as much as the initial supramolecular network formed.

If the stress on the network is not transferred to the covalent bonds until high strains, the cross-linker length series may be interesting for large deformations. We did start to observe a relative trend in the strain at break, increasing with increasing cross-linker length. The shorter cross-linkers showed a gel-to-sol transition between 200% and 400% strain, while the longer cross-linkers could withstand up to 500% strain on the rheometer (Figure S15e, Supporting Information). Since shear rheology becomes less accurate at high strains, we explored the mechanics in more depth with tensile testing. During uniaxial extension, the failure strain increased with increasing cross-linker length:  $\approx 225\%$  for short, 425% for 2K-PEG, and 550% for 5K-PEG (Figure 5a–c). Unfortunately, the 20K-PEG sample could not withstand the handling forces required reliably to fix the sample in the grips. Considering that the pre-crosslinked supramolecular hydrogel stretched very little (and could not withstand loading on the tensile tester), connecting the self-assembled structures through molecular bridges resulted in tunable stretchability correlated with the cross-linker length. We also observed that the tensile modulus was dependent on the cross-linker length with a larger modulus ( $\approx 25$  kPa) for the short cross-linker when compared to the two longer cross-linkers ( $\approx 2$ –5 kPa, Figure S16, Supporting Information). There were less clear trends for the work of extension across the series, yet the PEG5K cross-linker was the largest ( $55 \text{ kJ m}^{-3}$ , Figure S16, Supporting Information), suggesting that the longer cross-linker may allow more strain energy.

Next, we wished to investigate these supramolecular/covalent hydrogels further using compression testing, to understand their ability to withstand the compression forces found in many load-bearing tissues. We first tested the supramolecular hydrogel, since this was precluded from the tensile testing. A 10% w/v supramolecular hydrogel was observed to have an elastic compressive modulus of 7 kPa, while the strength and strain energy at 90% strain was 327 kPa and  $30.49 \text{ kJ m}^{-3}$ , respectively (Figure S17, Supporting Information). Then, after cross-linking (short dithiol, 1:1 ratio), this same sample exhibited an approximately tenfold increase in elastic compressive modulus (90 kPa), an approximately sevenfold increase in strength ( $\approx 2$  MPa), and an approximately sixfold increase in strain energy ( $180 \text{ kJ m}^{-3}$ , Figure 5d,e,f; Figure S17, Supporting Information). We also investigated the cross-linked hydrogel (using the short dithiol) at 5% w/v with a 1:1 and 1:0.25 ratio of [NB]:[thiol] in order to probe both the effect of concentration and cross-link density,

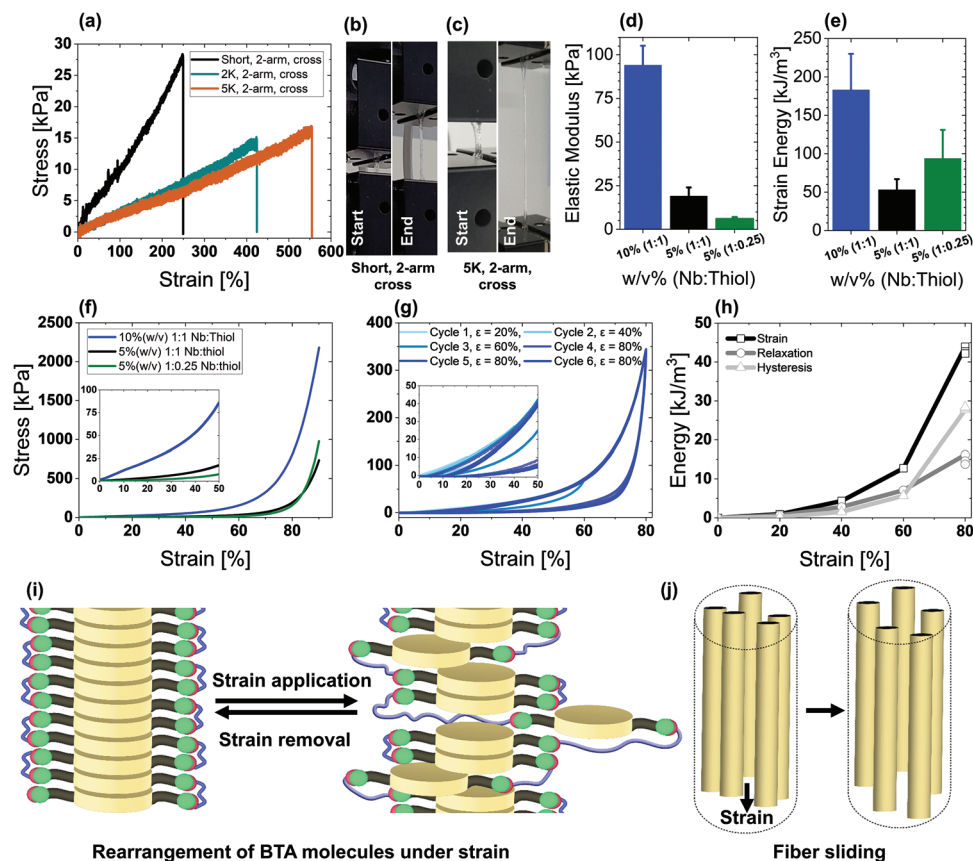


**Figure 5.** Mechanical properties of hydrogels before and after cross-linking. a–c) Stress–strain curves of the cross-linked hydrogels during a tensile test (a), and optical images of the short (b) and PEG 5K (c) hydrogels during the test. d,e) Elastic moduli (d) and strain energies (e) calculated from the compression tests. f) Compression stress–strain curves of the cross-linked hydrogels until 90% strain loaded at 1 mm min<sup>-1</sup> and released at 0.2 mm min<sup>-1</sup>. The same sample was reloaded immediately for the next cycle without any waiting time. g) Compression stress–strain curves for ramped cyclic loading of the 10% (w/v, 1:1 NB/thiol) cross-linked hydrogel of varying strain loaded at 1 mm min<sup>-1</sup> and released at 0.2 mm min<sup>-1</sup>. The same sample was reloaded immediately for the next cycle without any waiting time. h) Strain energy, relaxation energy, and hysteresis energy calculated for each cycle in the graph (g). Of note, three values from the triplicate 80% strain are shown in order to show the lack of fatigue in these cycles. i,j) Proposed mechanisms for energy dissipation during high strain loading include rearrangement of the network via mechanisms like BTA unstacking in BTA fibers (i) and BTA fiber sliding (j).

observing elastic moduli of 20 and 5 kPa and compressive strengths of  $\approx 0.5$  and  $\approx 1$  MPa, respectively (Figure 5d,e,f). These results indicated the ability to tune the compressive moduli as a function of both the concentration of the macromonomer and the concentration of the cross-linker. Important for tissue engineering applications, these elastic moduli (between 5 and 90 kPa) fall within the range observed for various native tissues,<sup>[75]</sup> and the compressive strengths ( $\approx 0.5$ – $2.5$  MPa) are within the range of biological tissues such as cartilage<sup>[76]</sup> and the human Annulus Fibrosus.<sup>[77]</sup>

During these compression tests, we noticed that the supramolecular hydrogels exhibited pseudoplastic deformation (Figure S17, Supporting Information, shown for 10% w/v), while none of the cross-linked hydrogels fractured even under 90% compression (Figure 5f). Visually, we observed elastic recovery rates corresponding to their moduli and cross-link density after these compression tests. Near instantaneous recovery was observed for the 10% (w/v, 1:1 [NB]:[thiol]), while the 5% (w/v, 1:1 [NB]:[thiol]) recovered  $\approx 93\%$  of its original height in under 2 min and the 5% (w/v, 1:0.25 [NB]:[thiol]) recovered greater than 90% of its height in 20–30 min. This elastic recovery behavior

can be expected since the covalent cross-links store energy elastically, and the elastic recovery can be enhanced with the increasing number of covalent cross-links.<sup>[18]</sup>

Seeing this clear trend in elastic recovery after the compression test, the combination of supramolecular and covalent cross-links were investigated for their ability to effectively dissipate energy in a reversible fashion. Performing cyclic loading from 20% to 80% strain revealed that the 10% 1:1 ratio hydrogel had enhanced hysteresis (area between loading and unloading curves) with increased strain, consistent with an effective dissipation mechanism. The loading cycle curves matched well, demonstrating elastic recovery and no appreciable change in the elastic modulus was observed (Figure 5g). Interestingly, during a constant strain of 80% in three consecutive cycles without any lapse time, the maximum stress and strain energy remains the same (Figure 5h) and no softening was observed,<sup>[78]</sup> which usually occurs in the classical double network<sup>[49]</sup> and hybrid hydrogels.<sup>[18]</sup> The data suggested that the supramolecular interactions are disrupted with the applied strain, yet were able to rapidly and reversibly recover without rupturing covalent bonds. Furthermore, while individual molecules may pull out of fibers during high



strain, fibril sliding (like in collagen fibrillar sliding<sup>[12]</sup>) could also contribute significantly to energy dissipation (Figure 5i,j). During this energy-dissipating rearrangement of the supramolecular polymers and network, the covalent bonds resist deformation by storing elastic energy and enabling elastic recovery. Using the above-proposed mechanism, we could also rationalize the bimodal stress–strain response observed during compression: a compliant response at low strains and a stiff response at higher strains like the load-bearing soft collagenous tissues.<sup>[79]</sup>

## 2.7. The Supramolecular and Cross-Linked Hydrogels Showed Similar Diffusion Coefficients

So far, our experiments have suggested that the topology of the underlying supramolecular hydrogel network after cross-linking is not noticeable at low deformation, yet is only discernible upon the application of larger amounts of force or strain. To further understand the nanoscale structure before and after cross-linking, we surmised that the diffusion coefficient should also remain relatively constant if there are no significant changes to the low-strain moduli. We turned to fluorescence recovery after photobleaching (FRAP) experiments with two different dextrans sizes (3–5 and 70 kDa) to probe this hypothesis. No significant difference in diffusion coefficient was observed between the supramolecular NB BTA hydrogel and those samples cross-linked with short dithiol or 2K-PEG (Figure 4f; Figure S18, Supporting Information). We did observe the normal decrease in diffusion coefficient as a function of the dextran size. Our observations differ from traditional covalent hydrogels in which network density and topology typically influence the diffusion coefficient of analytes;<sup>[80]</sup> however, our strategy closely mimics Nature's approach of cross-linking semi-flexible bundles of fibers with an open porous network without appreciable changes in the open structure.<sup>[81]</sup> Our results point to a similar mechanism in these synthetic supramolecular/covalent materials. Altering the topology and connectivity of the network on a molecular level is only seen at higher forces and strains, yet still allows the free diffusion of analytes throughout the sample.

## 2.8. The Supramolecular and Cross-Linked Hydrogels are Self-Healing

With a biomimetic and tough hydrogel in hand, we then proceeded to investigate the self-healing capability of the NB BTA hydrogels. Mainly, could the supramolecular self-assembly still impart self-healing, and what were the limits when subjected to covalent bond formation? Furthermore, self-healing is an important property required for hydrogels to quickly reform the network and maintain shape fidelity in a variety of applications from reprocessable materials, to injectability and 3D printing. The supramolecular NB BTA hydrogels (5% and 10% w/v) showed self-healing in under 2 min after cutting into two pieces and then pressing firmly together (Figure S19, Supporting Information). More quantitatively, the self-healing of the networks was investigated using shear rheology and determined to be within a few seconds (Figure S19, Supporting Information).

We subsequently determined the ability of hydrogels cross-linked with short dithiols to self-heal after 2 and 24 h (5% w/v

with dithiol 0.5, 1, and 2 equivalents, Figure 6a; Figures S20 and S21, Supporting Information). The hydrogels were cut into two pieces, which were then manually rejoined. While 1-mole equivalent provided little resistance to separation, 2-mole equivalents provided relatively more. The sample with 0.5-mole equivalents offered the most resistance and required repeated mechanical stretching to separate the two pieces. A similar trend was observed for longer time points; however, the self-healing was slightly more pronounced after 24 h and required more force to disrupt cohesion (1 equiv Movie S7, Supporting Information, 2 equiv Movie S8, Supporting Information, 0.5 equiv Movie S9, Supporting Information). The self-healing behavior of the cross-linked sample can be attributed to the reversible supramolecular associations of NB BTAs; however, it is worth noting that all samples eventually broke at the original defect. The samples with 0.5 and 2 molar equivalents likely showed better self-healing due to fewer covalent cross-links and more mobility of the supramolecular macromonomers within the hydrogel.

Finally, we investigated the self-healing of the hydrogels using the shear rheology of cross-linked hydrogels at 2.5%, 5%, and 10% w/v with an equimolar amount of short cross-linker (1:1 [NB]:[thiol]). In contrast to qualitative self-healing, the shear rheology showed near-instantaneous self-healing/recovery. We also tested the longer cross-links (2K-PEG-2-arm, 5K-PEG-2-arm, and 20K-PEG-2-arm) and found rapid self-healing (Figure S22, Supporting Information). In line with previous experiments, we find that self-healing kinetics on the rheometer do not translate well into macroscopic self-healing of hydrogel monoliths.

## 2.9. The NB BTA Supramolecular Hydrogels Exhibited Shear-Thinning Properties

Shear-thinning behavior is highly beneficial for injectability and bioprinting. Steady shear rheology was performed and viscosity as a function of shear rate was recorded. A continuous flow sweep for the 5% w/v NB BTA hydrogel showed a Newtonian plateau at the low shear rates and then a continuous and almost linear decrease in viscosity with an increasing shear rate (Figure 6b). A decrease in viscosity with increasing shear rate indicates the shear-thinning of the hydrogel. These rapid shear-thinning properties can be attributed to fast exchange rates (i.e., low lifetimes) of NB BTA molecules between fibers. This shear-thinning and self-healing forecasted a promising potential for these hydrogels in injectable and 3D bioprinting applications.

## 2.10. The NB BTA Hydrogel is Injectable, Possesses Yield Stress, and Creates Anisotropically Aligned Fibers after Injection and Cross-Linking

Knowing that the NB BTA hydrogel exhibits good self-healing and shear-thinning, we next moved to investigate the injectability of the hydrogel and the postinjection hydrogel morphology before and after cross-linking. For both the 5% and 10% w/v hydrogels, manual injection with a 22-gauge needle led to the extrusion of continuous filaments with good shape fidelity (Figure 6c; Figure S23 and Movie S6 in the Supporting Information for 5% hydrogel). Overall, the 5% hydrogel provided

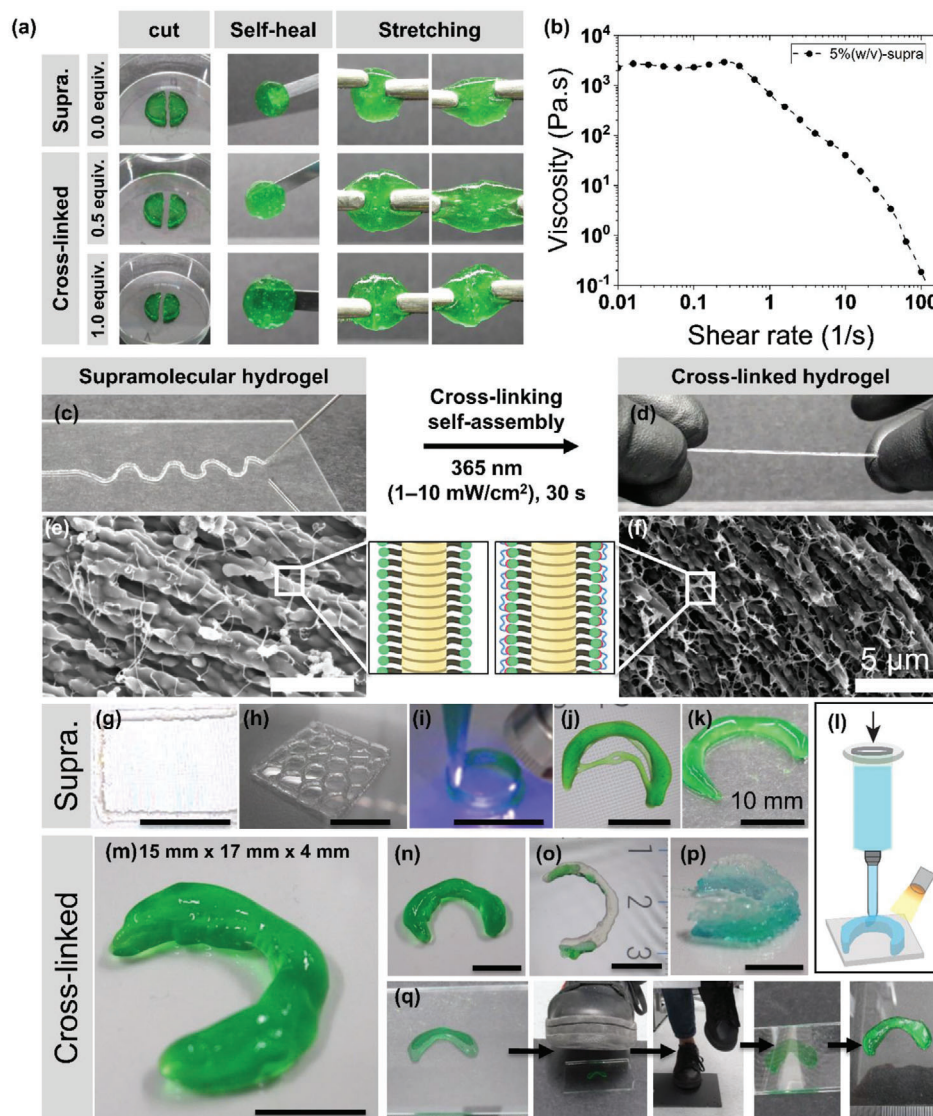


**Figure 6.** Self-healing, shear-thinning, injectability, and 3D printability of the NB BTA hydrogel. a) A self-healing visual test showed the self-healing behavior of hydrogels after 24 h in a closed environment. b) Decrease in viscosity with increasing shear rate showed shear-thinning behavior of the hydrogels. c) Extruding of supramolecular hydrogel (5% w/v) into a continuous uniform fiber with 1 equivalent of a short thiol cross-linker and  $2 \times 10^{-3}$  M LAP photoinitiator. The extruded fiber was cross-linked using 365 nm UV-light. d) The cross-linked fiber was observed to be strong and stretchable. e,f) Cryo-SEM images of non-crosslinked (e) and cross-linked (f) hydrogels after extruding through a 22 gauge syringe showed fibril morphology before and after cross-linking. g–i) The supramolecular hydrogel extruded into a single filament (g), hexagonal (h), and hollow tube structures (i). j,k) Hollow (j) and solid (k) meniscus cartilage models were 3D printed using the supramolecular hydrogel. l) Schematic of the 3D printing of a cartilage model using the extrusion printer. m,n) The meniscus cartilage model printed with 5% hydrogel, then cross-linked after printing each layer. o,p) A cartilage model printed with 5% hydrogel with inks with different equivalents of thiol cross-linker. The green ink (top part in o and bottom part in p) has a 1:1 ratio of NB to thiol and the clear ink (bottom part in o and top part in p) has a 1:0.5 ratio of NB to thiol. q) The meniscus cartilage model recovery before (left) and after (right) 60 kg of weight exerted three times.

easier injection (less pressure) and more continuous fiber formation upon injection compared to the 10%. The pressure required to initiate a flow, i.e., extrude these hydrogels indicated that the hydrogel possesses yield stress. Considering the low pressure required and continuous smooth filament formation, the 5% w/v hydrogel has more relevance for 3D printing. The Herschel–Bulkley model fitting resulted in a yield stress of 78 kPa. Next, we discovered that the extruded filament was stretchable after cross-linking (Figure 6d; Movie S6, Supporting

Information). These hydrogels can also be shaped upon injection; we were capable of extruding different institute names (BIOMATT, MERLN, CTR) by hand (Figure S23, Supporting Information).

The micron-scale structural features of the extruded gels were investigated after injection and before or after covalent cross-linking using cryo-SEM (Figure S23, Supporting Information). Of note these hydrogels are purely supramolecularly cross-linked before injection; the covalent reinforcement is only performed

after injection. The extruded supramolecular hydrogels showed anisotropically aligned bundles of fibers that were more compact and strongly bundled when compared to the nonextruded supramolecular hydrogel (vide infra, Figure 6e; Figure S24 in the Supporting Information). After cross-linking, the fiber bundles were slightly distorted, yet were largely retained as in previous experiments. Of note, during the sample preparation for cryo-SEM, the cross-linked hydrogel took a large amount of force to break, which could result in the observed nonuniform and distorted structures (Figure 6f; Figure S24, Supporting Information).

### 2.11. The NB BTA can be used as a Biomaterial Ink for the 3D Printing of a Cartilage Structure

After establishing that syringe-extruded hydrogel retained an aligned bundle morphology, hydrogels at 5% and 7.5% w/v were tested for 3D printing using pressure-based extrusion BIO X bioprinter. The hydrogel at 5% w/v displayed more continuous and uniform filaments compared to the 7.5% w/v hydrogel, and at a lower pressure (90 kPa for 5% w/v vs 200 kPa for 7.5% w/v).<sup>[63]</sup> Correspondingly, hydrogels at 5% w/v were used for 3D printing of a single filament, a grid-like structure, 6 layers of a hollow cube, a hexagonal structure, and then 8 layers of a circular hollow tube (Figure 6g–i). All of the structures were printed with uniform filaments and retained their shapes postprinting. Subsequently, a solid-tissue-like structure was printed, namely a 3D model of a human meniscus. The meniscus was chosen given the hydrogel's toughness and fast elastic recovery. A meniscus cartilage model (meniscus shape, 15×17 mm, 6 layers, and rectilinear infill pattern) was 3D printed (using the 5% w/v) into several meniscus shapes (Figure 6j,k; Figure S25, Supporting Information); in all cases, the hydrogel printed easily, the transitions from thick to thin edges were made smoothly, and the hydrogel shape remained stable postprinting.

Next, we investigated the effect of cross-linking on the resolution, retention of fine structural details, and mechanical robustness during printing. A meniscus was 3D printed using the 5% w/v hydrogel with the short dithiol cross-linker. The hydrogel was cross-linked by irradiation using 365 nm UV-light from 30 to 60 s between each layer (Figure 6l–n; Figure S26, Supporting Information). The 3D printed and cross-linked hydrogels retained fine details of the 3D cartilage model when compared to the supramolecular hydrogel (vide supra). To demonstrate toughness, the printed cartilage model was placed between two glass plates, and a student weighing 60 kg was placed on the plates for 30 s repeatedly (three times). After unloading, we observed that the hydrogel did not break and recovered more than 90% of its original height within 5 min (Figure 6q).

Tissues and especially tissue interfaces are rarely uniform. They often possess spatial gradients of mechanical properties; for example, the stiffness increases in cartilage tissue from the superficial soft zone to the calcified deep zone.<sup>[75]</sup> In line with this reality, we wondered if this platform could enable zonal gradients by printing using a layer-by-layer approach. Utilizing the self-healing capacity of our hydrogels, along with the knowledge that the equilibrium storage modulus can be tuned by changing

cross-linker mole equivalents (vide supra), we aimed to create a prototype of a zonal construct. Toward this aim, we created a NB BTA cartilage model with two different moduli by varying the short thiol cross-linker ratio while keeping the NB BTA 5% w/v constant. The different biomaterial inks were deposited at different sites on the cartilage model to show that the inks can be deposited spatially with desired mechanical properties. The printed gradient was then cross-linked as a single solid entity without any discontinuities or cracks (Figure 6o,p).

### 2.12. The NB BTA Hydrogels Maintained Cell Viability in Bulk, after Injection, and During Bioprinting

To evaluate the bioprintability of the NB BTA hydrogels, relevant for tissue engineering applications, we determined the cell viability of printed cell-laden hydrogels. Towards this aim, we chose to work with ATDC5 chondrocytes, a widely studied cell type for cartilage tissue engineering and cartilage-like matrix production. ATDC5s were encapsulated within the NB BTA hydrogels (5% w/v) and cell viability was observed in the supramolecular hydrogel before and after cross-linking (1:1 NB/thiol, schematically shown in Figure 7a). After 2 h, the hydrogels were stained with calcein-AM (green = live cell) and ethidium homodimer (red = dead cell) to determine cell viability. Quantification of the cells showed that >80% of cells were alive after 2 h in both the supramolecular and cross-linked hydrogel (Figure 7b,c; Figure S27, Supporting Information). Similar cell viability (>80% by manual counting and >90% of the total cell area) between the supramolecular and cross-linked samples demonstrated that exposure to the cross-linking conditions did not detrimentally affect the cell viability. Of note, we chose to quantify cell viability via the area of live-dead stain due to the prohibitive automation of this quantification in 3D, and the move by other groups to use this metric in 3D biofabrication techniques.<sup>[82]</sup>

Many studies have shown that shear-thinning and self-healing hydrogels protect cells from shear stresses during injection and extrusion bioprinting,<sup>[61,62,83]</sup> so we investigated the NB BTA hydrogel as a potential injectable cell carrier. ATDC5 cell-laden hydrogels (4% w/v) were extruded manually (using hand pressure) through a 22 gauge syringe (ID = 0.41 mm, schematically shown in Figure 7a), and cell viability was determined before and after cross-linking. We observed that >80% via cell counting and >90% via cell area were alive before and after cross-linking; this result suggested that cells remained highly viable in the NB BTA hydrogel after extrusion and the postextrusion cross-linking did not decrease cell viability (Figure 7d,e; Figure S27, Supporting Information).

After demonstrating that the NB BTA hydrogel was a suitable carrier for cell viability and extrusion, we investigated the bioprinting of a complex meniscus shape using a BIO X bioprinter (Figure 7f). Bioprinting (4% w/v) the same meniscus shape as above, yet now using a bioink with ATDC5 chondrocytes, allowed the determination of cell viability by staining with a live-dead assay at day 1, 5, and 11. We observed that the cells remained highly viable (green color: live cells) through day 11 (Figure 7g–j), providing confidence to pursue further bioprinting studies with this material.

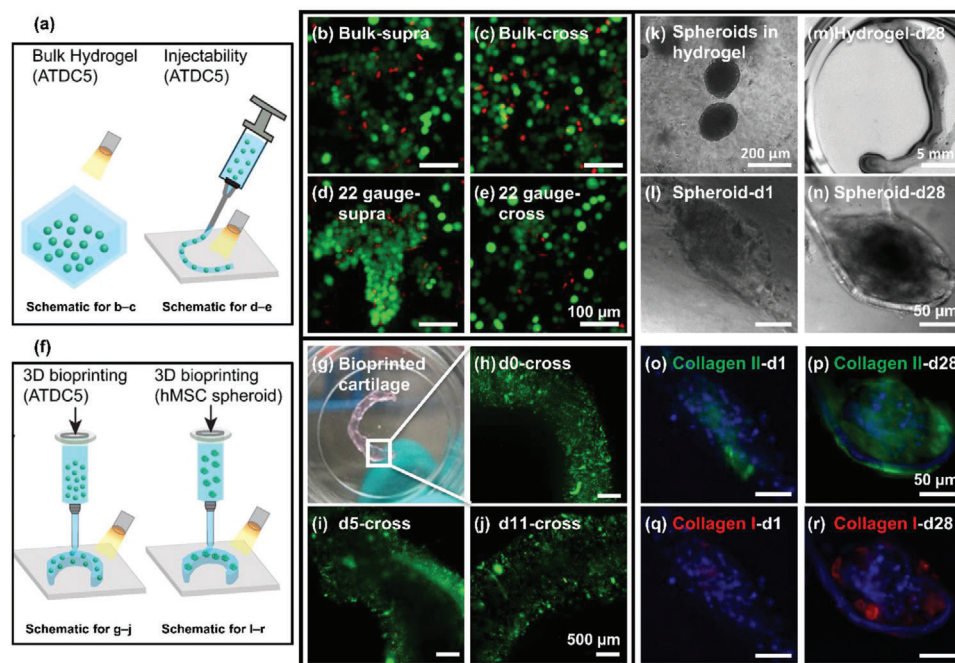


**Figure 7.** Cell viability after injectability and in 3D bioprinted hydrogels. a) Schematics representing the bulk hydrogel and injectability method employed for cell viability in (b)–(e). b,c) Live-dead images of ATDC5 chondrocytes in the supramolecular and cross-linked hydrogel after 2 h. The green color represents live cells and the red color represents dead cells. d,e) Live-dead images of ATDC5 chondrocytes after injection through 22 gauge after 2 h of injection. f) Schematics representing 3D bioprinting of chondrocytes and hMSC spheroids employed in (g)–(j) and (l)–(r), respectively. g) Visual image of the NB BTA hydrogel bioprinted cartilage construct. A cartilage model was printed using 22 gauge and with ATDC5s encapsulated. h–j) Live-dead images of cartilage model from day 0 until day 11. k) hMSC spheroids retain spherical morphology after mixing in NB BTA hydrogel. l–n) hMSC spheroid image after 1 d in culture (l), macroscopic hydrogel (cross-linked using short dithiol) picture (m), and spheroid picture (n) after 28 d in culture under chondrogenic differentiation conditions. o–r) Immunostaining for collagen II after 1 day (o) and 28 days (p) and immunostaining for collagen I after 1 day (q) and 28 days (r) of culture in bioprinted NB BTA hydrogel under chondrogenic differentiation conditions.

### 2.13. The NB BTA Hydrogel Supported Primary Cartilage-Specific Proteins in a Bioprinted Construct

Finally, we studied the potential of the biomimetic and tough NB BTA hydrogel with controlled degradability for the differentiation of human mesenchymal stromal cells (hMSCs) towards the chondrogenic lineage in a bioprinted scaffold. Here we chose to use hMSCs spheroids (mini tissue blocks, schematically shown in Figure 7f) as they are a promising platform for chondrogenic differentiation and have widespread therapeutic potential. Uniform hMSC spheroids were produced using a micro-molded nonadhesive agarose hydrogel (Figure S28, Supporting Information), then the encapsulated spheroids in the 4% w/v NB BTA hydrogel (Figure 7k) were bioprinted in a meniscus shape. In this study, we chose to introduce matrix metalloproteinase (MMP) degradable cross-links into the material (CGDG-VPLSLYSG-GDGC), which we observed created a biodegradable matrix for this supramolecular-covalent system (degradation shown in Figure S29 in the Supporting Information). In the final bioink, we employed a partially degradable (half MMP sensitive and half short dithiol cross-linker) and nondegradable (fully short dithiol) cross-linked bioinks in order to study the degradation capabilities of the bioprinted constructs. The spheroids remained stable and maintained their near-spherical morphology in both hydrogels; however, we did observe some elongation of the spheroids in the fully short dithiol hydrogel, likely due to

shear forces during extrusion (Figure 7l; Figure S30, Supporting Information). The bioprinted constructs were cultured under both basic and chondrogenic differentiation conditions through day 28. The hydrogel partially cross-linked with MMP-sensitive cross-linkers degraded in 14 d in the chondrogenic differentiation media and 21 d in the basic media (Figures S29 and S30, Supporting Information); however, the short dithiol cross-linked hydrogel stayed stable for 28 d in both the basic and chondrogenic media cultures at 37 °C (Figure 7m,n; Figure S31, Supporting Information). Degradation of these MMP-sensitive constructs in the presence of hMSCs spheroids indicated that the hMSCs were actively secreting MMP2 and MMP9 enzymes.

We then investigated the cartilage-specific protein production, i.e., collagen II in the surviving constructs. The presence of collagen II was observed clearly after day 28 (compared to day 1) in culture, and indicated the *in vitro* maturation and chondrogenic differentiation of the hMSCs (Figure 7o,p; Figure S32, Supporting Information). We also observed a very small amount of collagen I on day 1 and after day 28 in culture, usually on the outer edge of the spheroids (Figure 7q,r). In the negative control sample (after 28 d in basic medium), a limited amount of collagen II and collagen I were observed (Figure S32, Supporting Information). Overall, these results showed that the hMSC spheroids successfully produced collagen II, a cartilage-specific ECM protein, in the bioprinted NB BTA hydrogel scaffolds, and that the spheroids stayed stable and functional in the bioprinted constructs.

## 2.14. Outlook

Nature has extensively utilized the synergistic effect of combining 1D supramolecular fibril assembly with covalent cross-linking for designing materials with unique mechanical properties. Our findings suggest this ubiquitous, yet overlooked, strategy may be highly relevant in the design of synthetic biomaterials. Herein, we designed a synthetic hydrogel that combined the synergism of supramolecular assembly (first step) and covalent cross-linking (second step). The hydrogel mimicked the fibrous architecture of the native ECM, and the cross-linking of 1D supramolecular assemblies allowed tuning of the mechanical properties without affecting the fibrous morphology or diffusion of sample analytes through the material. Notably, the hydrogel platform allowed for tuning of the stiffness (5–100 kPa), toughness (50–180 kJ m<sup>-3</sup>), and strength (0.5–2 Mpa) of the hydrogels. The NB BTA hydrogel also exhibited room temperature recovery during ramped cyclic loading tests (between 20% and 80% strain), and no softening was observed. These NB BTA hydrogels were highly stretchable to ≈550% strain, and exhibited excellent shear-thinning, self-healing, and injectable properties. The reversible self-assembly in the supramolecular hydrogel enabled extrusion and 3D bioprinting, while the thiol-ene modification offered instantaneous cross-linking to retain sharp features on the printed construct. The supramolecular hydrogel can be 3D printed in many types of shapes ranging from a single filament to a complex cartilage model with good shape fidelity, with and without secondary cross-linking. Furthermore, the NB BTA hydrogel allowed the 3D printing of gradient, yet cohesive, structures with distinct mechanical properties such as stiffness and toughness, and can remove the need to print different materials with different cross-linking mechanisms for each bioink. While tough supramolecular hydrogels have been reported before, this is the first synthetic 1D fibrillar and tough supramolecular hydrogel with the capacity to be bioprinted into complex 3D structures. The NB BTA hydrogel exhibited excellent biocompatibility with chondrocytes (ATDC5) and supported hMSC differentiation to produce cartilage-specific proteins. In addition, just like in the natural ECM, we were able to engineer cell-mediated matrix degradation and remodelability by cross-linking with a MMP cleavable peptide cross-linker.

Our approach opens up a conceptual framework to tailor supramolecular interactions for the design of nanoscale architecture, followed by covalently (but reversible or degradable) fixing the hierarchical structure. This strategy provides access to supramolecular assemblies for obtaining (bio)materials with desired structures and mechanical properties previously unattainable by only supramolecular or covalent network strategies. Our approach thus can be generalized to build a 1D fibrous structure with a given set of structure–property relationships and can be expanded not only into the design of hydrogels within bioinks and biomaterials but also in numerous other applications where strength and structure are needed. For example, this approach can likely be generalized to other supramolecular polymers, and allows access to harnessing the specificity and reversibility of supramolecular interactions to design novel materials with unique architectures, multiple functionalities, and mechanical properties. Specific to bioinks, the design of modular inks with controlled structure, tunable mechanical properties,

and 3D bioprinting for creating spatiotemporal mechanical and biological gradients will be an exciting, challenging, and essential future step.

## 3. Experimental Section

**Materials:** All chemicals were purchased from Sigma-Aldrich unless otherwise stated. Bicyclo[2.2.1]hept-5-en-2-ylmethanamine, also known as, 5-norbornene-2-methylamine, a mixture of isomers, was purchased from TCI Chemicals. Silica gel (precoated 0.25 mm, 60-F254) was purchased from Merck. *N,N*-Diisopropylethylamine (DIPEA) used in the desymmetrization reaction was dried using sodium hydroxide pellets.

**Synthesis of Bis-Norbornyl Amide Mono-Pentafluoroester BTA Precursor (Perfluorophenyl 3,5-Bis((Bicyclo[2.2.1]hept-5-en-2-ylmethyl)Carbamoyl)Benzoate:** The bis-norbornyl amide mono-pentafluorophenyl ester was synthesized according to our previously published protocol and reproduced for this study.<sup>[72]</sup> In a dry, round-bottom flask, maintained under a nitrogen atmosphere tris(perfluorophenyl) benzene-1,3,5-tricarboxylate (510 mg, 0.720 mmol, 1 equiv.) was dissolved in 40 mL anhydrous dichloromethane (DCM). The above solution was cooled in a water-ice bath for 20 min and then a solution of anhydrous *N,N*-diisopropylethylamine (DIPEA) (376 μL, 2.16 mmol, 3 equiv.) in 18 mL anhydrous DCM was added into the reaction flask. Next, a solution of bicyclo[2.2.1]hept-5-en-2-ylmethanamine (186 μL, 1.44 mmol, 2 equiv.) in DCM (36 mL) was added drop-wise to the reaction flask in ≈20 min under nitrogen atmosphere. The reaction was stirred for 2 h at 4 °C, after which the reaction mixture was vacuum-dried to remove excess solvent. The desired molecule (perfluorophenyl 3,5-bis((bicyclo[2.2.1]hept-5-en-2-ylmethyl)carbamoyl)benzoate) (from crude) was separated on silica gel using eluent DCM/acetonitrile (92.5/7.5) by volume. The product was obtained as a white powder in a 52% (222 mg) isolated yield, and the <sup>1</sup>H NMR matched the previous report.<sup>[72]</sup>

**PEG20K-Bisamino Dodecane Synthesis:** PEG-bisamino dodecane was resynthesized according to our previously published protocol.<sup>[72]</sup> Briefly, in the first step, carbonyldiimidazole (CDI) activated PEG20K was synthesized by using bishydroxy PEG20K and CDI. In the second step, the polymer solution was added dropwise to the excess solution of 1,12 diaminododecane for creating PEG20K-bisamino dodecane. The final polymer was precipitated in excess diethyl ether and characterized using <sup>1</sup>H NMR.

**NB BTA Macromonomer Synthesis and Characterization:** In a dry, round-bottom flask, the BTA precursor (perfluorophenyl 3,5-bis((bicyclo[2.2.1]hept-5-en-2-ylmethyl)carbamoyl)benzoate) (0.25 g, 0.43 mmol, 2.2 equiv) was dissolved in 10 mL anhydrous DCM and DIPEA (101 μL, 0.58 mmol, 3 equiv) was added into the reaction flask. Subsequently, PEG20K bisaminododecane (4 g, 0.2 mmol, 1 equiv.) solution, dissolved in anhydrous DCM (10 mL) by vigorous stirring, was added dropwise to the reaction flask. The reaction mixture was stirred for 40 h at room temperature (≈20 °C) under a nitrogen atmosphere. Excess solvent was removed in vacuo and the crude reaction mixture was precipitated in excess cold diethyl ether twice and NB BTA macromolecule was obtained as a white powder in 94% yield (3.9 g). A second purification was done by dialyzing the sample in methanol against methanol to remove any unreacted small molecule impurities and the target compound was NB BTA obtained in 88% yield after the two step process. Gel permeation chromatography (GPC) analysis showed a molecular weight of around 23 000 g mol<sup>-1</sup> with a  $\bar{D}$  of 1.2. <sup>1</sup>H NMR shows the expected peaks and supports purity. <sup>1</sup>H NMR and GPC characterizations are shown in Figures S2 and S3 in the Supporting Information.

**Self-Assembly Studies Sample Preparation for Nile Red and cryo-TEM:** NB BTA (1, 2, and 5 mg) was weighed and dissolved in 50–100 μL methanol with the help of heating using a heat gun. The NB BTA solution in methanol was either injected into water or water was added into the methanol solution, and the final volume of the solution was adjusted to 1000 μL (1 mL). The solution was heated (until it become opaque using a heat gun) and vortexed. The same procedure was repeated two times and then the NB

BTA solution was placed on a heating plate maintained at 80 °C. The temperature was turned off for gradual cooling of the NB BTA solution to room temperature. The NB BTA solution was aged overnight (16–20 h) at room temperature before investigating Nile Red and cryo-TEM studies.

For cross-linking NB BTA self-assemblies, NB BTA at 5 mg mL<sup>-1</sup> was dissolved in 50–100 µL and then the total volume was adjusted to 900 µL. A similar heating, vortexing, and cooling procedure was repeated as above for supramolecular solutions. After overnight (16–20 h) aging of NB BTA solution at room temperature, LAP photoinitiator and cross-linker solutions in Milli Q water were added and the total volume was adjusted to 1000 µL. LAP final concentration was 2 × 10<sup>-3</sup> M and NB to thiol was in a 1:1 equimolar ratio to the amount of norbornene groups. The solution was cross-linked in a 365 nm UV oven at ≈1 mW cm<sup>-2</sup> for 1–4 min.

**Nile Red:** For Nile red studies, 200 µL sample was taken from the solutions prepared above for supramolecular assemblies at 1, 2, and 5 mg mL<sup>-1</sup>, and 3 µL Nile red solution (from a stock solution of 315 × 10<sup>-6</sup> M) was added to adjust final Nile red concentration to 5 × 10<sup>-6</sup> M. The samples, protected from light, were left at RT for a minimum of 30 min and fluorescence was recorded using a ClarioStar plate reader (BMG LabTech) nm) at excitation wavelength 500 nm and emission wavelength 550–740 nm.

Similarly, for the cross-linked sample at 5 mg mL<sup>-1</sup>, after exposure to UV, 3 µL Nile red solution was added to 200 µL of NB BTA solution prepared above and incubated for a minimum of 30 min. Nile red final concentration was 5 × 10<sup>-6</sup> M. The supramolecular NB BTA sample without a cross-linker was used as a control and also has Nile red final concentration of 5 × 10<sup>-6</sup> M.

**Cryo-TEM:** NB BTA sample was prepared either at 5 or 10 mg mL<sup>-1</sup> in water as described above in the self-assembly sample preparation section. The cryo-TEM experiments were performed on a FEI Technai 20. The grid preparation, sample vitrification, and imaging procedure was performed as described in the study.<sup>[72]</sup>

**Cryo-SEM:** Hydrogel samples were made in water at 4% and 5% wt using the heating-cooling procedure described below in the hydrogel formation section. High-pressure freezer planchettes were used to embed the hydrogel sample and the hydrogel sample was cooled in liquid Ethane. Very quickly, the sample was transferred to liquid nitrogen (–196 °C) and freeze-fractured by pulling the planchettes inside the liquid nitrogen bath. Using a vacuum cryo-transfer shuttle of the SCIOS system, the specimen carrier was transferred to the CRYO-SEM (SCIOS from FEI) and cooled to –187 °C. The sample was sputter-coated using in-built platinum coater. The cryo-scanning electron microscope was operated at an accelerating voltage of 2 kV.

**Hydrogel Formation:** NB BTA hydrogelator as solid polymer was weighed and added in a clear glass vial (size of 2–4 mL) and milli-Q water was added to adjust concentration to either 2.5%, 5%, and 10% w/v. Briefly, for 5% w/v, 10 mg of NB BTA hydrogelator was weighed in a glass vial and 200 µL of water was added and heated until the solution become opaque, due to the lower critical solution temperature (LCST ≈80 °C) of the PEG20K. Next, opaque solutions were vortexed. The same procedure was repeated twice. The hydrogel was centrifuged at 2000 g for around 10 min to ensure any residues on the glass walls settled down at the bottom of the glass vial. In the last step, the gel was cooled with a controlled decrease in temperature: the gel mixture was placed on a heating plate set to 80 °C and the temperature was turned off and the gels gradually cooled to lab temperature set to ≈20 °C.

For cross-linked hydrogels, the hydrogel was made initially at a higher concentration and aged overnight. The next day photoinitiator (LAP) and short thiol cross-linker solution were added to adjust the final concentration to 2.5%, 5%, and 10% w/v. For example, for 5% w/v and 1:1 ratio of norbornene to thiol for a short cross-linker, 10 mg were dissolved in 125 µL water (3.76 × 10<sup>-3</sup> M, 8% w/v initial concentration,) and the hydrogel was made with the above-described procedure heating, vortexing, and aging overnight. Then 25 µL of 3.76 × 10<sup>-2</sup> M of short thiol cross-linker, 25 µL of 1.60 × 10<sup>-2</sup> M of LAP photoinitiator solution, and 25 µL of Milli-Q water was added to adjust the final concentration of hydrogelator to 2.35 × 10<sup>-3</sup> M (5% w/v), LAP to 2 × 10<sup>-3</sup> M and short thiol final concentration to 4.7 × 10<sup>-3</sup> M. The hydrogel was broken and thoroughly mixed

with the LAP and cross-linker solutions and the hydrogel was then equilibrated between 1 and 3 h before cross-linking for uniform distribution of cross-linker.

For 2K, 5K, and 20K PEG dithiol cross-linkers, the same above procedure was repeated and for equimolar concentration, the required mass of the cross-linker was weighed; for example, 1.88 mg 2K dithiol was weighed and dissolved in 50 µL milli-Q water. The 2K dithiol solution and LAP photoinitiator solution (25 µL of 1.6 × 10<sup>-2</sup> M) was added to NB-BTA solution (125 µL of 3.76 × 10<sup>-3</sup> M, 8% w/v initial concentration) for adjusting concentration (× 10<sup>-3</sup> M) values as described above. The rest of the procedure was the same for making a hydrogel. For MMP-sensitive hydrogels, the cross-linker CGDGVPLS↓LYSGGDGC was used. The peptide cross-linker 1.4 mg was dissolved in 50 µL Milli-Q water and mixed with LAP photoinitiator solution and NB BTA polymer solution as described above. Final concentrations of different cross-linkers and NB BTA polymer for 1:1 ratio of thiol were adjusted based on the molecular weight of the thiol. For different ratios of NB to thiol, mole equivalents and the concentration of cross-linkers were adjusted accordingly.

**Rheology:** Rheological measurements were performed using a DHR-2 rheometer (TA instruments). We used 20 mm cone-plate geometry with a 2.002° angle. All measurements were performed at room temperature (≈20 °C). For removing any mechanical history, a rejuvenation protocol was performed, which was composed of a strain amplitude sweep until 400–1000% strain (at frequency 1 rad s<sup>-1</sup>) for rupturing the network followed by a time sweep (at 1% strain) for observing aging kinetics. Oscillatory strain amplitude sweeps from 1% to 1000% was carried out at an angular frequency of 1 rad s<sup>-1</sup>. A frequency sweep was performed at 1% oscillation strain ranging from 0.1 to 627 rad s<sup>-1</sup>. Self-healing measurements, in the first step network, were ruptured at 400% strain followed by a recovery phase at 1% strain. A minimum of 3 cycles were done for the self-healing test. Cross-linking of hydrogel was performed in a time sweep at 1% strain and 10 rad s<sup>-1</sup> using UV light intensity of ≈10 mW cm<sup>-2</sup>. For observing shear-thinning behavior, ascending logarithmic flow sweeps were carried out. Viscosity and shear stress were recorded as a function of shear rate and the shear rate was increased from 0.01 to 500 s<sup>-1</sup>. Per decade, 10 points were recorded and equilibration time and averaging time were set to 5 and 30 s, respectively.

**Uniaxial Compressive Tests:** All uniaxial compressive tests were performed at room temperature using the Shimadzu AGSX universal mechanical testing instrument equipped with a 500 N load cell. Hydrogel specimens for mechanical testing were prepared using cylindrical-shaped PDMS molds with a diameter of 10 mm and height of 2 mm or a diameter of 8 mm and height of 3 mm. The round PDMS mold was placed inside 12 well plates and then the mold was filled with hydrogel using a spatula. The well plate was covered with the lid and centrifuged at 3000 g to remove any possible trapped air bubbles. The well plate lid was covered with parafilm and stored overnight in the fridge at 4 °C before testing to avoid any water evaporation. A preload force of 0.01–0.2 N was applied to ensure good contact between hydrogel and compression plate. Each sample was deformed to 90% strain at a constant strain rate of 1 mm min<sup>-1</sup>. Cross-linked hydrogel tests were carried out in triplicate and supramolecular gel at 5% w/v and 10% was done in duplicate. Elastic modulus was calculated as the slope of the stress–strain curve between either 0–10% or 0–20% strain region since correlation stays linear.

**Cyclic Compression Tests:** To characterize the mechanical behavior of the materials in the loading condition close to the working conditions and to evaluate the reversible behavior of hydrogels and their ability to recover, besides the compression measurements, multiple cyclic loading-unloading compression experiments were performed using the Shimadzu AGSX universal mechanical testing instrument equipped with a 500 N load cell. The specimens were compressed to 20% of the initial height in the first cycle at a deformation speed of 1 mm min<sup>-1</sup> and then released immediately at the velocity of 0.2 mm min<sup>-1</sup>. Then, the strain progressively increased to 40%, 60%, and 80% in the following cycles. Moreover, three cycles of compression were applied from 0% to 80% strain. Strain energy and relaxation energy were calculated by the integration of the areas under the curve for a given strain cycle.

**Uniaxial Tensile Tests:** All uniaxial tensile tests were performed at room temperature using the Shimadzu AGSX universal mechanical testing instrument equipped with a 500 N load cell. Hydrogel samples were prepared in dog bone PMMA molds (dimensions  $L = 26$  mm,  $W = 2$  mm,  $D = 4$  mm). All the tensile tests were repeated at least 3 times and each hydrogel was stretched at a strain rate of  $5 \text{ mm min}^{-1}$  until failure.

**Fluorescence Recovery after Photobleaching (FRAP):** Hydrogels of 200  $\mu\text{L}$  in volume were prepared in 4-chamber 35 mm glass-bottom dishes (D35C4-20-0-N, Cellvis), 1 mL of FITC-labelled dextran solution (3–5 or 70 kDa at  $0.1 \text{ mg mL}^{-1}$ , Sigma-Aldrich, FD4-250MG and 46945-100MG-F) was added and incubated overnight at  $4^\circ\text{C}$  in the dark. Fluorescent recovery after photobleaching (FRAP) imaging was performed on a Leica TCS SP8 STED using the FRAP modules of Leica Application Suite X software (LAS X FRAP). FRAP bleaching was performed on a z-height of 40  $\mu\text{m}$  in each hydrogel. Parameters were set as followed: bleaching point of 60  $\mu\text{m}$  diameter, pre/post bleaching laser at 5%/ 488 nm/ 800 gain, and a time per frame of 0.223 s. After 5 frames prebleach (1.2 s), samples were bleached for 90 frames (21.2 s), and fluorescent recovery was gathered for 400 frames postbleaching (110.5 s). ROI data were extracted in Fiji ImageJ-win64. Area and mean grey values were obtained for the bleach, total and background ROIs. The obtained values were imported into the open-source application FrapBot<sup>[84]</sup> to obtain the  $\tau_{1/2}$  (half-time) of the fluorescent recovery curve. Obtained  $\tau_{1/2}$  was used to calculate the diffusion coefficients by the Soumpasis equation, with  $D =$  diffusion coefficient,  $r =$  radius of the bleaching area, and  $\tau_{1/2} =$  the halftime of recovery (Equation 1). Statistical analysis was performed in GraphPad Prism 8.2.0, one-way ANOVA

$$D = 0.224 \left( \frac{r^2}{\tau_{1/2}} \right) \quad (1)$$

**Printing:** NB BTA hydrogels, without photoinitiator, at a final concentration of 5% w/v was tested. To investigate printability, the extrusion-based BioX bioprinter (CellInk, Sweden) was used. All printing was performed at room temperature. Conical plastic needles (VIEWEG GmbH, Germany) were fixed to 3 mL syringes with a 22 gauge nozzle diameter (ID = 0.41 mm). The pressure applied to form a continuous filament depends on the hydrogel formulation, which was around 90 kPa. The infill density was set to 100% and the distance from the needle to the print surface was optimized so that the leading edge of the flow was in line with the needle. To explore the printability of NB BTA hydrogels, 4 structures were printed: (a zigzag path, 10 mm in width and 32 mm in length), a 3-layer hollow cube (10 mm in width and length and 2 mm in height), grid-like structures (two layers  $10 \times 10$  grid, 15 mm in width and length), and 3D meniscus (10.8 mm x 8.9 mm x 1.4 mm). Printability tests were carried out using a plastic petri dish as the printing surface. We then imaged each print (16-megapixel camera) and used ImageProPlus (MediaCybernetic, USA) software to threshold images and measure dimensions.

**Degradation Mass Loss Studies:** The cross-linked hydrogel was made following the procedure mentioned in the hydrogel formation section above. Hydrogel cross-linked with short dithiol (1:1 ratio of NB to thiol), MMP sensitive dithiol (1:1 ratio of NB to thiol), and cross-linked with the 0.5-mole equivalent of short thiol and the 0.5-mole equivalent of MMP sensitive thiol cross-linker was made. Degradation was studied in DMEM media without FBS and with 10% FBS. Degradation media has 200  $\text{ng mL}^{-1}$  of type IV collagenase (MMP-2 and MMP-9) until day 3 and then increased to 500  $\text{ng mL}^{-1}$  from day 3 to day 20. Collagenase IV concentration was increased for accelerating degradation since hydrogel barely degraded until day 3 in 200  $\text{ng mL}^{-1}$  collagenase IV. The hydrogel was taken out of the media, and extra water on the surface was cleaned with tissues and then the wet weight of the hydrogel was recorded at days 1, 2, 3, 4, 7, 10, 13, 20. Data for each sample is normalized to day 1 for calculating mass loss percentage (%) or degradation over 20 d. The mass loss % of the hydrogel was quantified using the following equation.

$$\text{Mass loss (\%)} = \frac{m_i - m_1}{m_1} \quad (2)$$

Where  $m_i$  is the wet mass at a specific time point and  $m_1$  is the wet mass of the gel after 24 h in DMEM.

**ATDC5 Chondrocytes Cell Culture:** ATDC5 cells were cultured at  $37^\circ\text{C}$  in a humidified incubator with 5%  $\text{CO}_2$ . Chondrocytes cell culture media for ATDC5 expansion consists of Gibco® DMEM/F-12 (1:1) with no glutamine, and with 10% fetal bovine serum, and 1% P/S. ATDC5 were passaged at 75–80% confluent. Using 0.05% trypsin-EDTA cells were detached and washed with PBS. Cells were re-suspended in the required amount of chondrocyte cell culture media for encapsulation in hydrogels.

**ATDC5 Cell Encapsulation in NB BTA Hydrogel and Bioink Preparation:** Chondrocytes (RIKEN cell bank, Japan) were encapsulated in NB BTA hydrogel at a concentration of 5 million (M) cells per mL of hydrogelator. For cell culture studies, the hydrogel was prepared in DMEM/F-12 (1:1) with 1% Penicillin–Streptomycin (P/S) at an initial concentration of 8% w/v following the method described in the hydrogel-making section above. The next day cell suspension was added to adjust the final concentration to 4% w/v for supramolecular hydrogel. For cross-linked hydrogel, LAP photoinitiator, cross-linker solution, and cell suspension were added to adjust the final concentration to 4% w/v. For example, NB BTA was dissolved in 375  $\mu\text{L}$  DMEM (with 1% P/S) at the initial concentration of 8% w/v ( $3.76 \times 10^{-3} \text{ M}$ ). The next day, short thiol 75  $\mu\text{L}$  of  $3.76 \times 10^{-2} \text{ M}$  and 75  $\mu\text{L}$  of  $1.6 \times 10^{-2} \text{ M}$  LAP solution were added and mixed by breaking the hydrogel. After equilibration, a time of  $\approx 2$  h, cell suspension in 225  $\mu\text{L}$  was mixed in hydrogel using the self-healing method described below. For mixing cell suspension in the hydrogel, a uniform hydrogel layer covering an entire surface area of the well plate (48-well plate, nonadherent) was made by centrifugation at 2000 g. Cell suspension in DMEM was uniformly spread on top of the hydrogel, and another layer of the same hydrogel was added on top of the previous layer. After a waiting time of 5–10 min when two layers are self-healed, the gel was broken gently into small pieces using a spatula and put the pieces together to ensure uniform cell distribution. After a waiting time of  $\approx 30$  min in a sterile flow hood, which allows sufficient self-healing of small pieces of hydrogel, in the presence of cell suspension, the hydrogel was transferred to a 3 mL sterile syringe for injectability and bioprinting. Thiol to NB was in 1:1 ratios and short thiol final concentration was  $3.76 \times 10^{-3} \text{ M}$ , and NB BTA final concentration was  $1.88 \times 10^{-3} \text{ M}$ . LAP photoinitiator final concentration was  $1.6 \times 10^{-3} \text{ M}$ .

**Cell Culture Conditions and Production of hMSC Spheroids:** Human mesenchymal stromal cells (hMSC, 8F3543, Lonza) were expanded in alpha MEM medium with GlutaMAX (32561-029, Gibco) supplemented with 10% v/v of fetal bovine serum (FBS, F7524, Sigma-Aldrich) by culturing 3000 cells  $\text{cm}^{-2}$  until they reached 70% of confluence up to passage 5, at  $37^\circ\text{C}$  under a 5%  $\text{CO}_2$  atmosphere. The microwell array insert used to produce hMSC spheroids was previously described.<sup>[85]</sup> Briefly,  $5 \times 10^5$  cells were seeded in each microwell array to obtain 164 spheroids containing an average of 3048 cells each. The cells were cultured in these arrays ( $37^\circ\text{C}$ , 5%  $\text{CO}_2$  atmosphere) until day 5 to form highly spherical spheroids. The culture medium was refreshed every 48 h.

**MSC Spheroids Encapsulation for Bioink Preparation:** The hMSC spheroids were collected from the microwell array inserts, washed twice with PBS, and mixed into the hydrogel. Two types of hydrogel were used for the encapsulation of spheroids; a hydrogel cross-linked fully with short thiol and a 0.5-short:0.5-MMP hydrogel which is partially cross-linked with short thiol (0.5-mole equivalent) and partially with MMP sensitive cross-linker (0.5-mole equivalent). Around 2500 hMSCs spheroids were mixed per milliliter of hydrogel, giving a total cell suspension of around  $7.6 \times 10^6$  cells  $\text{mL}^{-1}$ . A similar procedure of bioink preparation was repeated for the short thiol cross-linker as described above for chondrocytes.

For a 0.5-short:0.5MMP hydrogel volume of 750  $\mu\text{L}$ , 30 mg NB BTA polymer was dissolved in 375  $\mu\text{L}$  of MEM (1% P/S) at an initial concentration of 8% w/v ( $3.76 \times 10^{-3} \text{ M}$ ), and hydrogel was aged overnight. The next day, 38  $\mu\text{L}$  of short and 38  $\mu\text{L}$  of MMP-sensitive cross-linker, each with an initial concentration of  $3.76 \times 10^{-2} \text{ M}$ , and 75  $\mu\text{L}$  of LAP with  $1.6 \times 10^{-2} \text{ M}$  initial concentrations were mixed in the hydrogel by breaking the hydrogel. After an equilibration time of  $\approx 1$  h, MSC spheroids suspension in 225  $\mu\text{L}$  DMEM was mixed with hydrogel with described steps above

in the procedure of bioink preparation for chondrocytes. Each cross-linker and NB BTA polymer have a final concentration of  $1.88 \times 10^{-3}$  M in the hydrogel. LAP final concentration in the hydrogel was  $1.60 \times 10^{-3}$  M.

**Injectability:** The ATDC5-laden hydrogel was transferred to a sterile 3 mL syringe and then injected through a 22 gauge conical needle. Hydrogels were cross-linked using UV light at  $\approx 1$  mW  $\text{cm}^{-2}$  between 30 and 60 s.

**Bioprinting:** After MSC spheroids were encapsulated within hydrogels, 3D meniscus structures (stl file, 10.8 mm x 8.9 mm x 1.4 mm) were printed using the BioX extrusion printer (CellInk, Sweden). All printing was performed at room temperature. Conical plastic needles (VIEWEG GmbH, Germany) were fixed to 3 mL syringes with a 22 gauge nozzle diameter (ID = 0.41 mm). The pressure applied to form a continuous filament was 90 kPa. The infill density was set to 100% and the distance from the needle to the print surface was optimized so that the leading edge of the flow was in line with the needle.

**Morphological Analysis of Spheroids after Mixing and Bioprinting Process Over 28 d:** To evaluate the impact of the bioprinting and spheroid encapsulation inside the hydrogel cross-linked with short thiol cross-linker and 0.5-short and 0.5-MMP sensitive cross-linkers, bioprinted constructs were cultured for up to 28 d in alpha MEM basic medium and chondrogenic differentiation medium. Images of the constructs were taken using an optical microscope (Eclipse Ti-E Nikon, Japan) after the bioink preparation step, and on days 3, 7, 14, 21, and 28 after bioprinting.

**Chondrogenic Differentiation Performed on Bioprinted Constructs:** First, the validation of hMSCs used in this work for chondrogenic differentiation was confirmed according to the published protocol by Penick et al.<sup>[86]</sup> Then, spheroid-based bioprinted constructs were differentiated for 28 days in a post-bioprinting process as previously described by Decarli et al.<sup>[87]</sup> using a chondrogenic culture medium initially defined by Johnstone et al.<sup>[88]</sup> with some modifications. The chondrogenic culture medium was freshly prepared every week and composed of 4.5 g  $\text{L}^{-1}$  high-glucose DMEM medium (31966-021, Gibco) supplemented with 50 mg  $\text{mL}^{-1}$  of Insulin-Transferrin-Selenium (ITS premix, 41400-045, Gibco, USA), 40 mg  $\text{mL}^{-1}$  of proline (P5607, Sigma-Aldrich), 57.8  $\mu\text{g mL}^{-1}$  of ascorbic acid (A8960, Sigma),  $0.1 \times 10^{-6}$  M of dexamethasone (D8893, Sigma-Aldrich), 10 ng  $\text{mL}^{-1}$  of TGF- $\beta$ 1 (100-21, PeproTech) and 1% v/v of P/S.

**Cell Viability (Live/Dead):** LIVE/DEAD Viability/Cytotoxicity Kit from Thermofisher (Netherlands) was used for evaluating cell viability. ATDC5 cultured gels were transferred to a glass-bottom well plate, and a solution of calcein-AM (final concentration  $1 \times 10^{-6}$  M) and ethidium homodimer-1 (EthD-1, final concentration  $2 \times 10^{-6}$  M) was added to cover the whole gel. The gels were incubated for 45 min in the dark at 37 °C and imaged using an inverted fluorescence microscope (Nikon Eclipse Ti-E microscope, Japan). Live and dead cell area was quantified using image J. At places where cells were clumped together and formed aggregates they were counted as one cell in ImageJ analysis, and this could affect the ratio between live and dead cell numbers. To overcome this we calculated the area of live and dead cells.

**Immunohistochemical Analysis:** Immunohistochemical analysis was performed to determine the presence of collagen types I, II, and nuclei. The assays were performed in fixed samples containing the whole bioprinted constructs. Due to the complex composition of the spheroid-based constructs, some modifications were implemented in the immunostaining procedure to ensure efficient stain penetration throughout the sample, as previously described.<sup>[87]</sup> Briefly, the primary antibodies anti-mouse collagen-I (Abcam 6308), and anti-rabbit collagen-II (Abcam 34 712) diluted in 1% BSA and 0.05% Tween-20 in PBS (1:200) were used. The incubation with the first antibody was performed overnight at 4 °C. The samples were washed three times with PBS and incubated with the secondary antibody diluted (1/500) in the same buffer for 1 h at room temperature. After three washes, samples were incubated with 4',6-diamidino-2-phenylindole (DAPI) for DNA stain (1:100) for 1 h and 15 min, at room temperature. The samples were then analyzed on a glass slide using a fluorescence microscope (Nikon Eclipse Ti-E microscope, Japan).

## Supporting Information

Supporting Information is available from the Wiley Online Library or from the author.

## Acknowledgements

S.H. and C.v.B. would like to thank the European Research Council (ERC) for funding under the European Union's Horizons 2020 research and innovation programme (Grant Agreement No. 694801). M.C.D. and L.M. acknowledge the support of the European Union's Horizon 2020 research and innovation programme under grant agreement No 953169 (Inter-Lynk). A.A.A., L.M., and M.B.B. would like to thank the support of NWO (Innovation Fund Chemistry, project "DynAM" under project agreement 731.016.202). A.A.A. would like to thank the support of Marie Skłodowska-Curie Individual Fellowships under grant agreement 101028471. F.A.A.R. and M.B.B. would like to thank RegMedXB for support. A.A., M.E., L.M.P., and M.B.B. would like to thank the Research Foundation-Flanders (FWO) under contract G080020N. We would also like to thank V. Lapointe for support in the FRAP measurements for this study.

Note: Figure 5 was reset on September 1, 2023, after initial publication online.

## Conflict of Interest

S.H., A.A., L.M., and M.B.B. are co-inventors on a patent submission based upon these findings.

## Data Availability Statement

The data that support the findings of this study are openly available in DataVerse at <https://doi.org/10.34894/AFBYVF>, reference number 1.

## Keywords

bioprinting, covalent capture, dynamic hydrogels, Supramolecular self-assembly, tissue engineering

Received: February 8, 2023  
Revised: April 25, 2023  
Published online: July 30, 2023

- [1] F. Gattazzo, A. Urciuolo, P. Bonaldo, *Biochim. Biophys. Acta* **2014**, *1840*, 2506.
- [2] H. W. Ooi, S. Hafeez, C. A. Van Blitterswijk, L. Moroni, M. B. Baker, *Mater. Horiz.* **2017**, *4*, 1020.
- [3] S. Correa, A. K. Grosskopf, H. L. Hernandez, D. Chan, A. C. Yu, L. M. Stapleton, E. A. Appel, *Chem. Rev.* **2021**, *121*, 11385.
- [4] M. P. Lutolf, J. L. Lauer-Fields, H. G. Schmoedel, A. T. Metters, F. E. Weber, G. B. Fields, J. A. Hubbell, *Proc. Natl. Acad. Sci. USA* **2003**, *100*, 5413.
- [5] R. K. Das, V. Gocheva, R. Hammink, O. F. Zouani, A. E. Rowan, *Nat. Mater.* **2016**, *15*, 318.
- [6] O. Chaudhuri, L. Gu, D. Klumpers, M. Darnell, S. A. Bencherif, J. C. Weaver, N. Huebsch, H. P. Lee, E. Lippens, G. N. Duda, D. J. Mooney, *Nat. Mater.* **2016**, *15*, 326.
- [7] O. Chaudhuri, J. Cooper-White, P. A. Janmey, D. J. Mooney, V. B. Shenoy, *Nature* **2020**, *584*, 535.
- [8] A. Chrisnandy, D. Blondel, S. Rezakhani, N. Brogiere, M. P. Lutolf, *Nat. Mater.* **2021**, *21*, 479.



- [9] Z. Álvarez, A. N. Kolberg-Edelbrock, I. R. Sasselli, J. A. Ortega, R. Qiu, Z. Syrgiannis, P. A. Mirau, F. Chen, S. M. Chin, S. Weigand, E. Kiskinis, S. I. Stupp, *Science* **2021**, 374, 848.
- [10] F. L. C. Morgan, J. Fernández-Pérez, L. Moroni, M. B. Baker, *Adv. Healthcare Mater.* **2022**, 11, 2101576.
- [11] K. Zhang, Q. Feng, Z. Fang, L. Gu, L. Bian, *Chem. Rev.* **2021**, 121, 11149.
- [12] U. G. K. Wegst, H. Bai, E. Saiz, A. P. Tomsia, R. O. Ritchie, *Nat. Mater.* **2015**, 14, 23.
- [13] A. H. Kang, J. Gross, *Proc. Natl. Acad. Sci. USA* **1970**, 67, 1307.
- [14] M. J. Buehler, *Proc. Natl. Acad. Sci. USA* **2006**, 103, 12285.
- [15] D. R. Eyre, M. A. Paz, P. M. Gallop, *Annu. Rev. Biochem.* **1983**, 53, 717.
- [16] J. Ozsvar, C. Yang, S. A. Cain, C. Baldock, A. Tarakanova, A. S. Weiss, *Front. Bioeng. Biotechnol.* **2021**, 9, 643110.
- [17] K. Djinić-Carugo, P. Young, M. Gautel, M. Saraste, *Cell* **1999**, 98, 537.
- [18] J. Y. Sun, X. Zhao, W. R. K. Illeperuma, O. Chaudhuri, K. H. Oh, D. J. Mooney, J. J. Vlassak, Z. Suo, *Nature* **2012**, 489, 133.
- [19] S. Hong, D. Sycks, H. F. Chan, S. Lin, G. P. Lopez, F. Guilak, K. W. Leong, X. Zhao, *Adv. Mater.* **2015**, 27, 4035.
- [20] J. P. Gong, Y. Katsuyama, T. Kurokawa, Y. Osada, *Adv. Mater.* **2003**, 15, 1155.
- [21] X. Hu, M. Vatankehah-Varnoosfaderani, J. Zhou, Q. Li, S. S. Sheiko, *Adv. Mater.* **2015**, 27, 6899.
- [22] L. Xu, C. Wang, Y. Cui, A. Li, Y. Qiao, D. Qiu, *Sci. Adv.* **2019**, 5, eaau3442.
- [23] Z. Han, P. Wang, Y. Lu, Z. Jia, S. Qu, W. Yang, *Sci. Adv.* **2022**, 8, 5066.
- [24] M. Guo, L. M. Pitet, H. M. Wyss, M. Vos, P. Y. W. Dankers, E. W. Meijer, *J. Am. Chem. Soc.* **2014**, 136, 6969.
- [25] Z. Wang, X. Zheng, T. Ouchi, T. B. Kouznetsova, H. K. Beech, S. Av-Ron, T. Matsuda, B. H. Bowser, S. Wang, J. A. Johnson, J. A. Kalow, B. D. Olsen, J. P. Gong, M. Rubinstein, S. L. Craig, *Science* **2021**, 374, 193.
- [26] J. Kim, G. Zhang, M. Shi, Z. Suo, *Science* **2021**, 374, 212.
- [27] C. Norioka, Y. Inamoto, C. Hajime, A. Kawamura, T. Miyata, *NPG Asia Mater.* **2021**, 13, 34.
- [28] M. J. Webber, E. A. Appel, E. W. Meijer, R. Langer, *Nat. Mater.* **2015**, 15, 13.
- [29] O. J. G. M. Goor, S. I. S. Hendrikse, P. Y. W. Dankers, E. W. Meijer, *Chem. Soc. Rev.* **2017**, 46, 6621.
- [30] M. B. Baker, A. W. Bosman, M. A. J. Cox, P. Y. W. Dankers, A. Dias, P. Jonkheijm, R. Kietlyka, *Tissue Eng. – Part A* **2022**, 28, 511.
- [31] T. Aida, E. W. Meijer, S. I. Stupp, *Science* **2012**, 335, 813.
- [32] L. E. R. O’Leary, J. A. Fallas, E. L. Bakota, M. K. Kang, J. D. Hartgerink, *Nat. Chem.* **2011**, 3, 821.
- [33] T. Schnitzer, G. Vantomme, *ACS Cent. Sci.* **2020**, 6, 2060.
- [34] Z. Yu, F. Tantakitti, T. Yu, L. C. Palmer, G. C. Schatz, S. I. Stupp, *Science* **2016**, 351, 497.
- [35] S. M. Chin, C. V. Synatschke, S. Liu, R. J. Nap, N. A. Sather, Q. Wang, Z. Álvarez, A. N. Edelbrock, T. Fyrner, L. C. Palmer, I. Szleifer, M. Olvera De La Cruz, S. I. Stupp, *Nat. Commun.* **2018**, 9, 2395.
- [36] C. Li, A. Iscen, H. Sai, K. Sato, N. A. Sather, S. M. Chin, Z. Álvarez, L. C. Palmer, G. C. Schatz, S. I. Stupp, *Nat. Mater.* **2020**, 19, 900.
- [37] M. A. Khalily, M. Goktas, M. O. Guler, *Org. Biomol. Chem.* **2015**, 13, 1983.
- [38] L. Aulisa, H. Dong, J. D. Hartgerink, *Biomacromolecules* **2009**, 10, 2694.
- [39] M. Fernández-Castaño Romera, X. Lou, J. Schill, G. Ter Huurne, P. P. K. H. Franssen, I. K. Voets, C. Storm, R. P. Sijbesma, *J. Am. Chem. Soc.* **2018**, 140, 17547.
- [40] J. Liu, C. S. Y. Tan, Z. Yu, Y. Lan, C. Abell, O. A. Scherman, *Adv. Mater.* **2017**, 29, 1604951.
- [41] A. A. Aldana, S. Houben, L. Moroni, M. B. Baker, L. M. Pitet, *ACS Biomater. Sci. Eng.* **2021**, 7, 4077.
- [42] J. Fang, A. Mehlich, N. Koga, J. Huang, R. Koga, X. Gao, C. Hu, C. Jin, M. Rief, J. Kast, D. Baker, H. Li, *Nat. Commun.* **2013**, 4, 2974.
- [43] R. Freeman, M. Han, Z. Álvarez, J. A. Lewis, J. R. Wester, N. Stephanopoulos, M. T. McClendon, C. Lynsky, J. M. Godbe, H. Sangji, E. Luijten, S. I. Stupp, *Science* **2018**, 362, 808.
- [44] A. N. Edelbrock, T. D. Clemons, S. M. Chin, J. J. W. Roan, E. P. Bruckner, Z. Álvarez, J. F. Edelbrock, K. S. Wek, S. I. Stupp, A. N. Edelbrock, S. I. Stupp, T. D. Clemons, Z. Álvarez, J. F. Edelbrock, S. M. Chin, J. J. W. Roan, E. P. Bruckner, K. S. Wek, *Adv. Sci.* **2021**, 8, 2004042.
- [45] W. E. M. Noteborn, D. N. H. Zwagerman, V. S. Talens, C. Maity, L. van der Mee, J. M. Poolman, S. Mytnyk, J. H. van Esch, A. Kros, R. Eelkema, R. E. Kietlyka, *Adv. Mater.* **2017**, 29, 1603769.
- [46] B. O. Okesola, H. K. Lau, B. Derkus, D. K. Boccorh, Y. Wu, A. W. Wark, K. L. Kiick, A. Mata, *Biomater. Sci.* **2020**, 8, 846.
- [47] A. E. Way, A. B. Korpusik, T. B. Dorsey, L. E. Buerkle, H. A. Von Recum, S. J. Rowan, *Macromolecules* **2014**, 47, 1810.
- [48] Y. Wang, Z. Xu, M. Lovrak, V. A. A. le Sage, K. Zhang, X. Guo, R. Eelkema, E. Mendes, J. H. van Esch, *Angew. Chemie – Int. Ed.* **2020**, 59, 4830.
- [49] C. B. Rodell, N. N. Dusaj, C. B. Highley, J. A. Burdick, *Adv. Mater.* **2016**, 28, 8419.
- [50] F. L. C. Morgan, L. Moroni, M. B. Baker, *Adv. Healthcare Mater.* **2020**, 9, 1901798.
- [51] C. L. Hedegaard, A. Mata, A. Mata, *Biofabrication* **2020**, 12, 032002.
- [52] A. Lee, A. R. Hudson, D. J. Shiwerski, J. W. Tashman, T. J. Hinton, S. Yerneni, J. M. Bliley, P. G. Campbell, A. W. Feinberg, *Science* **2019**, 365, 482.
- [53] L. A. Hockaday, K. H. Kang, N. W. Colangelo, P. Y. C. Cheung, B. Duan, E. Malone, J. Wu, L. N. Girardi, L. J. Bonassar, H. Lipson, C. C. Chu, J. T. Butcher, *Biofabrication* **2012**, 4, 035005.
- [54] D. B. Kolesky, R. L. Truby, A. S. Gladman, T. A. Busbee, K. A. Homan, J. A. Lewis, *Adv. Mater.* **2014**, 26, 3124.
- [55] B. Grigoryan, S. J. Paulsen, D. C. Corbett, D. W. Sazer, C. L. Fortin, A. J. Zaita, P. T. Greenfield, N. J. Calafat, J. P. Gounley, A. H. Ta, F. Johansson, A. Randles, J. E. Rosenkrantz, J. D. Louis-Rosenberg, P. A. Galie, K. R. Stevens, J. S. Miller, *Science* **2019**, 364, 458.
- [56] M. A. Skylar-Scott, S. G. M. Uzel, L. L. Nam, J. H. Ahrens, R. L. Truby, S. Damaraju, J. A. Lewis, *Sci. Adv.* **2019**, 5, eaaw2459.
- [57] A. Ghanizadeh Tabriz, M. A. Hermida, N. R. Leslie, W. Shu, *Biofabrication* **2015**, 7, 045012.
- [58] S. M. Hull, C. D. Lindsay, L. G. Brunel, D. J. Shiwerski, J. W. Tashman, J. G. Roth, D. Myung, A. W. Feinberg, S. C. Heilshorn, *Adv. Funct. Mater.* **2021**, 31, 202007983.
- [59] S. M. Bakht, M. Gomez-Florit, T. Lamers, R. L. Reis, R. M. A. Domingues, M. E. Gomes, *Adv. Funct. Mater.* **2021**, 2104245, 2104245.
- [60] L. Ouyang, J. P. K. Armstrong, Y. Lin, J. P. Wojciechowski, C. Lee-Reeves, D. Hachim, K. Zhou, J. A. Burdick, M. M. Stevens, *Sci. Adv.* **2020**, 6, eaabc5529.
- [61] H. Wang, D. Zhu, A. Paul, L. Cai, A. Enejder, F. Yang, S. C. Heilshorn, *Adv. Funct. Mater.* **2017**, 27, 1605609.
- [62] J. Lou, F. Liu, C. D. Lindsay, O. Chaudhuri, S. C. Heilshorn, Y. Xia, *Adv. Mater.* **2018**, 30, 1705215.
- [63] S. Hafeez, H. Ooi, F. Morgan, C. Mota, M. Dettin, C. van Blitterswijk, L. Moroni, M. Baker, *Gels* **2018**, 4, 85.
- [64] C. B. Highley, C. B. Rodell, J. A. Burdick, *Adv. Mater.* **2015**, 27, 5075.
- [65] C. Loebel, C. B. Rodell, M. H. Chen, J. A. Burdick, *Nat. Protoc.* **2017**, 12, 1521.
- [66] C. B. Rodell, A. L. Kaminski, J. A. Burdick, *Biomacromolecules* **2013**, 14, 4125.
- [67] N. A. Sather, H. Sai, I. R. Sasselli, K. Sato, W. Ji, C. V. Synatschke, R. T. Zambrotta, J. F. Edelbrock, R. R. Kohlmeier, J. O. Hardin, J.

- D. Berrigan, M. F. Durstock, P. Mirau, S. I. Stupp, *Small* **2021**, *17*, 2005743.
- [68] H. H. Susapto, D. Alhattab, S. Abdelrahman, Z. Khan, S. Alshehri, K. Kahin, R. Ge, M. Moretti, A. H. Emwas, C. A. E. Hauser, *Nano Lett.* **2021**, *21*, 2719.
- [69] A. C. Farsheed, A. J. Thomas, B. H. Pogostin, J. D. Hartgerink, *Adv. Mater.* **2023**, *35*, 2210378.
- [70] S. Hafeez, A. Aldana, H. Duimel, F. A. A. Ruiten, M. C. Decarli, V. Lapointe, C. van Blitterswijk, L. Moroni, M. B. Baker, *Adv. Mater.* **2023**, *35*, 2207053.
- [71] C. M. A. Leenders, T. Mes, M. B. Baker, M. M. E. Koenigs, P. Besenius, A. R. A. Palmans, E. W. Meijer, *Mater. Horiz.* **2014**, *1*, 116.
- [72] S. Hafeez, H. W. Ooi, D. Suylen, H. Duimel, T. M. Hackeng, C. van Blitterswijk, M. B. Baker, *J. Am. Chem. Soc.* **2022**, *144*, 4057.
- [73] M. C. A. Stuart, J. C. Van De Pas, J. B. F. N. Engberts, *J. Phys. Org. Chem.* **2005**, *18*, 929.
- [74] C. M. A. Leenders, M. B. Baker, I. A. B. Pijpers, R. P. M. Lafleur, L. Albertazzi, A. R. A. Palmans, E. W. Meijer, *Soft Matter* **2016**, *12*, 2887.
- [75] C. F. Guimarães, L. Gasperini, A. P. Marques, R. L. Reis, *Nat. Rev. Mater.* **2020**, *5*, 351.
- [76] M. A. Slivka, N. C. Leatherbury, K. Kieswetter, G. G. Niederauer, *Tissue Eng.* **2001**, *7*, 767.
- [77] G. D. O'Connell, S. Sen, D. M. Elliott, *Biomech. Model. Mechanobiol.* **2012**, *11*, 493.
- [78] K. M. Schmoller, A. R. Bausch, *Nat. Mater.* **2013**, *12*, 278.
- [79] J. A. Stella, A. D'Amore, W. R. Wagner, M. S. Sacks, *Acta Biomater.* **2010**, *6*, 2365.
- [80] E. Axpe, D. Chan, G. S. Offeddu, Y. Chang, D. Merida, H. L. Hernandez, E. A. Appel, *Macromolecules* **2019**, *52*, 6889.
- [81] D. C. Schoenmakers, A. E. Rowan, P. H. J. Kouwer, *Nat. Commun.* **2018**, *9*, 2172.
- [82] P. N. Bernal, P. Delrot, D. Loterie, Y. Li, J. Malda, C. Moser, R. Levato, *Adv. Mater.* **2019**, 1904209, 1904209.
- [83] L. M. Marquardt, V. M. Doulames, A. T. Wang, K. Dubbin, R. A. Suhar, M. J. Kratochvil, Z. A. Medress, G. W. Plant, S. C. Heilshorn, *Sci. Adv.* **2020**, *6*, eaaz1039.
- [84] R. Kohze, C. E. J. Dieteren, W. J. H. Koopman, R. Brock, S. Schmidt, *Cytom. Part A* **2017**, *91*, 810.
- [85] M. C. Decarli, M. V. de Castro, J. A. Nogueira, M. H. T. Nagahara, C. B. Westin, A. L. R. de Oliveira, J. V. L. da Silva, L. Moroni, C. Mota, Â. M. Moraes, *Biomater. Adv.* **2022**, *135*, 112685.
- [86] K. J. Penick, L. A. Solchaga, J. F. Welter, *BioTechniques* **2005**, *39*, 687.
- [87] M. C. Decarli, A. Seijas-Gamardo, F. L. C. Morgan, P. Wieringa, M. B. Baker, J. V. L. Silva, Â. M. Moraes, L. Moroni, C. Mota, *Adv. Healthc. Mater.* **2023**, *1*, 2203021.
- [88] B. Johnstone, T. M. Hering, A. I. Caplan, V. M. Goldberg, J. U. Yoo, *Exp. Cell Res.* **1998**, *238*, 265.